SUBMISSION TO CANADIAN GEOTECHNICAL JOURNAL

DATE:

02/07/2019

TITLE:

Shallow penetrometer tests – Theoretical and experimental modelling of the rotation stage

AUTHOR:

Schneider, M.A.[1], Stanier, S.A.[2], White, D.J.[3] and Randolph, M.F.[4]

POSITION AND AFFILIATION:

[1] Research Student, Centre for Offshore Foundation Systems, University of Western Australia

[2] University Senior Lecturer, Cambridge University Engineering Department, Trumpington Street, Cambridge, CB2 1PZ.

[3] Professor, University of Southampton (also affiliated to the University of Western Australia)

[4] Professor, Centre for Offshore Foundation Systems, University of Western Australia

CONTACT ADDRESS:

Dr Sam Stanier
Cambridge University Engineering Department
Trumpington Street
Cambridge
CB2 1PZ
United Kingdom

NUMBER OF WORDS, FIGURES AND TABLES:

Words: ~6200
Figures: 13
Tables: 4

KEYWORDS:

Shallow penetrometer; offshore engineering; in-situ testing; axial sliding resistance; pipe-soil interaction

SHALLOW PENETROMETER TESTS – THEORETICAL AND EXPERIMENTAL MODELLING OF THE ROTATION STAGE

Schneider, M.A., Stanier, S.A., White, D.J. and Randolph, M.F.

ABSTRACT

Shallow penetrometers are a new type of device that measures the properties of surficial offshore sediments via multi-phase tests involving penetration, dissipation and rotation stages. In fine grained soils such as silts and clays, these testing stages yield undrained strength, consolidation and interface friction properties relevant to subsea pipeline and shallow foundation design. This paper describes the fundamentals of the rotation stage, including models required for data interpretation, encompassing both a total and an effective stress framework. Additionally, new relationships to evaluate the pore pressure scaling factor, which is a key interpretation parameter required to convert discrete measurements of pore pressure on the penetrometers to an average pore pressure over the contact area, are developed based on large deformation finite element simulations. Results from an experimental campaign using kaolin clay samples are presented, illustrating the potential of the devices to rapidly and repeatably measure interface friction properties of fine-grained sediments offshore. The results compare well with comparative measures obtained from shear box tests conducted at similarly low effective stress levels. Recommendations regarding future in-situ applications are given at end of the manuscript.

INTRODUCTION

Accurate characterisation of near-surface soil properties is increasingly important for the development of offshore subsea infrastructure, such as seabed pipelines, cables and shallow foundations. The shear strength profile of soft surficial sediments over the upper half metre of the seabed may be assessed with conventional in-situ testing methods (e.g. cone, T-bar or ball penetrometer), with appropriate allowance for relatively shallow embedment. However, such devices provide very limited insight into the interface friction properties of soil. Also, laboratory element tests (e.g. simple or direct shear or triaxial tests) on near-surface samples are difficult because of the challenges of recovering and testing such soft soil specimens in the laboratory without sample disturbances (Clayton et al., 1998; Hover et al., 2013).

Shallow penetrometers overcome these limitations and can be used for in-situ testing in a recovered box-core on deck of a vessel. The hemiball and toroid penetrometer are two such sensor concepts (Yan et al., 2011; Stanier & White, 2014), which are capable, in principle, of determining strength, consolidation and interface friction properties at shallow embedment via tests comprising penetration, dissipation and rotation phases. A further advantage of the penetrometers is that direct assessment of the effective stress failure envelope is possible, since excess pore pressures are monitored continuously throughout the test at various locations on the penetrometers.

This paper describes and validates the rotation phase of shallow penetrometer tests and defines the test types that allow the full range of design parameters to be determined. These parameters mirror the requirements of industry guidelines that relate to pipelines, such as DNVGL-RP-F114 (Det Norske Veritas, 2017). A companion paper (Schneider et al., 2019b) provides a more detailed device description and covers back-analysis methods for the penetration and dissipation phases. In this paper, a comprehensive experimental campaign is reported, using tests in kaolin clay, along with results from finite element analyses to validate the interpretation approach.

The test campaign explored different test protocols, allowing the approaches for interpretation of the rotation phase to be validated, in terms of both total and effective stress interpretation frameworks. The finite element results were used to establish a scaling approach between the excess pore pressure measured at point locations on the device and the average excess pore pressure acting on the contacting surface. This scaling allows an effective stress interpretation of the interface behaviour during all test phases, regardless of the drainage condition.

Overall, the study demonstrates the potential of the box-core sized penetrometers for rigorous measurement of near-surface soil properties in soft soils.

SHALLOW PENETROMETERS

A detailed description of the box-core scale shallow penetrometers is given in the companion paper (Schneider et al., 2019b) and in Schneider et al. (2019a). Figure 1 shows a cross section for both the hemiball (D = 100 mm) and the pipe-shaped toroid (D = 25 mm) penetrometers. The former includes pore pressure transducers at three locations on the penetrometer interface: at invert (abbr. *inv*); intermediate (abbr. *int*); and midface positions (abbr. *mf*). Two transducers are provided at both the intermediate ($\theta = \pi/8$ or 22.5°) and midface ($\theta = \pi/4$ or 45°) locations for measurement redundancy. The four transducers installed on the toroid are all located at the tip of the penetrometer (invert) since the small device cross-section of 25 mm precludes the use of other locations.

The toroid has a lever arm to diameter ratio, L/D, of 2, which is sufficiently large to eliminate interference across the penetrometer section (Yan et al., 2011). The bearing and sliding response is therefore the same as for a straight pipe of the same diameter. The devices are actuated using a 2 degree-of-freedom electro-mechanical actuator described in Schneider et al. (2019a).

EXPERIMENTAL PROGRAMME

Sample preparation and soil characterisation

The testing campaign was performed in four containers of kaolin clay (390 mm × 1300 mm in plan) that were consolidated from slurry in a large consolidometer. A surface pressure of ~20 kPa was used, to reach a soil strength profile representative of offshore at shallow depths. The results of miniature T-bar tests as well as the moisture content measured in soil specimens recovered at different depths (using a miniature core sampler) revealed that all four samples were highly homogenous with a strength of ~1.5-1.75 kPa. This gave confidence in comparing data from shallow penetrometer tests performed in different soil samples. Additional information regarding the sample preparation and the soil characterisation process can be found in the companion paper (Schneider et al., 2019b).

Shallow penetrometer tests

Different variations of the rotation stage following undrained penetration and load-controlled consolidation (Schneider et al., 2019b) were investigated. A brief overview of the testing programme, for both the hemiball and toroid penetrometer, is provided in Table 3.

Shear box tests at low stress levels

For comparison and validation purposes the strength envelope for the kaolin-penetrometer coating interface was determined via conventional means. Interface shear box (ISB) testing is the de-facto standard laboratory test method for estimating pipeline-soil interface friction (White et al., 2015a; Westgate et al., 2018). Therefore, a rough interface for the shear box was manufactured using the same approach as for the penetrometer coating, which was to shot-blast a piece of Delrin plastic.

The interface tests involved very slow shearing at 0.05 mm/min, ensuring drained conditions, and were executed at very low effective stress levels (σ'_n ~ 5-15 kPa) similar to those achieved

in the shallow penetrometer tests. It was necessary to consider corrections, following Lehane & Liu (2013), to account for the effect of system friction for cases with and without soil ingress between the two halves of the shear box apparatus. Due to uncertainty regarding soil ingress, the two correction assumptions provided by Lehane & Liu (2013) are used (approach 1: no soil ingress; and approach 2: soil ingress between upper and lower halves of shear box). This provides a range of interpreted interface friction angle, which represents the uncertainty associated with performing ISB tests at low stress levels (see later Figure 6). Post-test observations indicated the presence of some clay in between the two halves of the shear box, which suggests correction approach 2 (soil squeezed into gap between shear boxes) to be more suitable. A minor stress level dependency was detected, as often observed at such low stress levels (Lehane & Liu, 2013; Meyer et al., 2015) but the determined interface friction angle is relatively constant (approach 2: $\delta \sim 20°$).

Additionally, conventional direct shear box tests (without an interface) were performed to check whether the surface finish of the penetrometer interface was sufficiently rough that the full friction angle of the kaolin was mobilised (Schneider et al., 2019a). These tests confirmed that the friction mobilised by the roughened Delrin plastic inserts is practically identical to the results derived from the standard shear box tests, showing that the penetrometer interface can be treated as 'fully rough' (i.e. $\delta = \phi'$).

INTERPRETATION OF ROTATION RESPONSE

This section describes the interpretation methods used to link the measured data during a rotation stage to the underlying interface / soil parameters.

The rotational response of a shallow penetrometer test is interpreted to estimate the following properties: undrained interface strength, $s_{u,int}$, drained interface friction angle, δ, and the operative consolidation coefficient, c_v, during that phase. For a 'fully rough' interface, these

strengths correspond to the internal soil properties. The undrained strength ratio ($s_{u,int}/\sigma'_{no}$) can then be determined, where σ'_{no} is the effective stress applied by the shallow penetrometer at the start of the rotation stage. If the soil is normally-consolidated (NC) under this stress, then the strength ratio corresponds to the fundamental property, the NC strength ratio $R = (s_{u,int}/\sigma'_{no})_{nc}$. The drained interface friction angle can also be determined in terms of the effective stress interface friction coefficient $\mu' = \tan\delta$.

Since pore water pressures are monitored throughout the test, interpretation methods based on an effective stress framework are possible. This allows the failure envelope in effective stress space to be determined – in addition to the conventional total stress analysis. The following subsections describe (i) the geometric factors used to convert the force and torque on the penetrometer into the interface stresses, (ii) the total stress back-analysis approach, (iii) the effective stress back-analysis approach and (iv) how mean pore pressures are determined, allowing the effective stress approach to be applied regardless of the drainage condition.

Geometric factors: effective radius, wedging and embedment

To interpret shallow penetrometer tests it is necessary to convert the measured torque, T, and vertical force, V, (which is held constant during rotation) into the average shear stress, τ_{ave}, and normal stress, $\sigma_{n,ave}$, on the surface of the penetrometer. This conversion depends on a wedging factor, ζ, the effective radius of the device, r_{eff}, and the penetrometer-soil contact area A_c, with

$$\tau_{ave} = \frac{(T/r_{eff})}{A_c} \qquad and \qquad \sigma_{n,ave} = \frac{N}{A_c} = \frac{\zeta V}{A_c} \tag{1}$$

The effective radius is the lever arm at which the torque resulting from τ_{ave} acts and is taken as constant for the toroid ($r_{eff,Toroid} = L = 2D$), but varies with embedment, w, (or the semi-angle of the embedded segment, θ_m) for the hemiball according to

$$r_{eff,Hemiball} = \frac{D \sin\theta_m}{3} \qquad with \qquad \theta_m = \cos^{-1}\left(1 - 2w/D\right) \tag{2}$$

The wedging factor, ζ, is the ratio between the total normal force on the penetrometer-soil contact, N, and the applied vertical load, V. White & Randolph (2007) derived an analytical solution for the wedging factor on a pipeline assuming a normal contact stress that varies with the cosine of the semi-angle θ (Figure 1), thus implying a reduction of normal contact stress with increasing distance from the penetrometer invert. The pipeline solution can be adopted for the toroid, since the ratio $L/D = 2$ is sufficient to exclude interference across the device (Yan et al., 2011), so that

$$\zeta_{Toroid} \simeq \zeta_{Pipeline} = \frac{2 \sin\theta_m}{\theta_m + \sin\theta_m \cos\theta_m} \leq 1.27 \tag{3}$$

Yan (2014) adopted similar assumptions to develop a wedging factor for the hemiball:

$$\zeta_{Hemiball} = \frac{3 \sin^2\theta_m}{2\left(1 - \cos^3\theta_m\right)} \leq 1.50 \tag{4}$$

Additionally, Yan (2014) reported empirical relationships derived from SSFE-simulations of the rotation stage, for both the hemiball and toroid penetrometer, which yielded very similar values to Equations (3) and (4). These simulations revealed that there is no significant change in wedging factor during the rotation phase.

The contact surface area, A_c, is a function of the semi-angle of the embedded segment, θ_m, and can be evaluated as:

$$A_{c,Hemiball} = \pi\left[\left(\frac{\sin\theta_m D}{2}\right)^2 + w^2\right] \quad or \quad A_{c,Toroid} = 2\pi DL\cos^{-1}\left(\frac{D-2w}{D}\right) \tag{5}$$

The parameters ζ, $r_{eff,Hemiball}$ and A_c all vary with penetrometer embedment, w. When the device penetrates deeply into the soil, the effective embedment, w' – i.e. the vertical height from the invert to the point where the soil leaves contact with the penetrometer (Figure 1) – is smaller than the position of the invert below the original soil surface (which is the embedment inferred from the actuator movement, w). The divergence occurs due to the soil being squeezed out radially. Based on repeated observations of this effect – visually and from pore pressure data – the effective embedment is derived by capping the semi-angle of the embedded segment at a value ($\theta_{m,cap}$) of π/4 for the toroid and π/3 for the hemiball. Throughout this study, the wedging factors, effective radius and contact area were estimated using the effective embedment (i.e. $w' = \min(w, w_{cap} = f(\theta_{m,cap}))$, thus capping the embedment recorded by the actuator once the embedment limit, w_{cap}, stated above is reached) in conjunction with the Equations (2), (3), (4), and (5).

Total stress interpretation method

The total stress interpretation method allows the undrained and drained interface strength properties to be identified, along with the transition in resistance from the initial (undrained) value to the final (drained) limit.

The interface friction coefficient $\mu = \tau_{ave}/\sigma_{n,ave}$, is calculated from the measured quantities as:

$$\mu = \frac{\tau_{ave}}{\sigma_{n,ave}} = \frac{T}{r_{eff} V \zeta} \tag{6}$$

For the undrained part of the total stress interpretation method to apply, there must be minimal excess pore pressure remaining from the penetration stage and any vertical unloading step when the rotations begins, so that $\sigma_{n,ave} = \sigma'_{n,ave}$. If any significant excess pore pressure remains, the effective stress on the interface will be lower than $\sigma_{n,ave}$, and the effective stress interpretation must be used.

The measured friction at the drained (μ_{dr}) and undrained (μ_u) limits can be linked to the underlying interface strength properties, δ and $s_{u,int}$, by

$$\mu_{dr} = \mu' = \tan\delta = \left(\frac{T}{r_{eff} V \zeta}\right)_{dr} \quad ; \quad \mu_u = \left(\frac{s_{u,\mathrm{int}}}{\sigma'_{no}}\right) = \left(\frac{T}{r_{eff} V \zeta}\right)_{u} \tag{7}$$

Note that for normally consolidated conditions, the undrained friction ratio, μ_u, will equate to the normally consolidated interface strength ratio *R*. The effect of over-consolidation on the interface strength can be explored by varying the vertical load prior to the rotation stage. By sustaining a higher vertical load while pore pressures dissipate, followed by unloading and further dissipation, the value of $s_{u,int}$ measured during the rotation stage will reflect an over-consolidated condition. To capture this effect, the equivalent undrained limit of Equation (7) can be rewritten in a SHANSEP or critical state form (Ladd et al., 1977; Wroth, 1984) as

$$R = \left(\frac{s_{u,\mathrm{int}}}{\sigma'_{no}}\right)_{nc} = \frac{\mu_u}{OCR^m} = \frac{T}{r_{eff} V \zeta \, OCR^m} \qquad with \qquad m \approx 1 - \frac{\kappa}{\lambda} \tag{8}$$

In this case the undrained interface strength model has two parameters: the NC strength ratio, $R = (s_{u,int}/\sigma'_{no})_{\mathrm{nc}}$ and the index *m*, with the latter linked to the plastic and elastic volumetric stiffnesses in the Cam clay model, λ and κ. Since the interface friction ratio has two soil properties, *R* and *m*, it is necessary to make two or more measurements of $(s_{u,int}/\sigma'_{no})$ at different values of *OCR* in order to identify both properties. The *OCR* term and the *m* parameter can be neglected in the case of normally consolidated interface conditions (see also Equation 7). Equation (8) is essentially valid for a fully rough penetrometer interface, as is the case here. However, the relation becomes increasingly less appropriate for smoother interface conditions due to the non-linear development of excess pore pressures with stress ratio.

During the rotation stage, the measured friction transitions from μ_u to μ_{dr}. This transition, when plotted against dimensionless time, $T_{rot} = c_v t/D^2$, tracks the consolidation 'backbone curve' (Figure 2), expressed by Randolph et al. (2012) for subsea pipelines as

$$\mu = \mu_{dr} - \left(\mu_{dr} - \mu_u\right) 0.5^{(T_{rot}/T_{rot,50})^n} \tag{9}$$

$T_{rot,50}$ is the non-dimensional time required to generate friction half way between the drained and undrained limits. Based on finite element simulations, Yan (2014) showed that $T_{rot,50}$ varies linearly with embedment from ~0.020-0.170 or ~0.004-0.03 as w/D increases from 0-0.5 for the toroid or hemiball, respectively, and n is a shape fitting parameter that varies from 0.7 to 1.0.

Effective stress interpretation method

The normal stress, $\sigma_{n,ave}$, acting at the interface between the device and the soil, can be combined with the average excess pore pressure, Δu_{ave}, in order to interpret the response in terms of effective stresses, regardless of the drainage condition. It is necessary, however, to apply a scaling factor β to the point measurements, Δu_{pos}, recorded at a specific transducer locations, to represent the average excess pore pressure across the contact area, so that

$$\sigma'_{n,ave} = \sigma_{n,ave} - \Delta u_{ave} = \frac{\zeta V}{A_c} - \beta \Delta u_{pos} \tag{10}$$

Using the above approach, the failure envelope of the interface, $\tau = f(\sigma'_n)$, can be assessed directly by plotting the full test data in τ-σ'-space. In this way, the results of a single test allow the failure envelope to be defined over a range of effective stress compared to the single value of effective stress applied in an interface shear box test. A similar analysis has been presented previously for instrumented model pipe tests (White et al., 2010a; Ballard et al., 2013).

Pore pressure scaling factor

SSFE wished-in-place simulations (Yan, 2014) suggested that the scaling factor $\beta = \Delta u_{ave} / \Delta u_{pos} \sim 0.65\text{-}0.80$, where the pore pressure u_{pos} is measured at the invert position of the penetrometers. These investigations require extension to cover the hemiball, which features pore pressure transducers at two additional locations: the midface ($\theta = \pi/4$ or 45°) and intermediate locations ($\theta = \pi/8$ or 22.5°), for which no solutions have been published to date.

During trial tests, the excess pore pressures recorded at the spot measurement locations (invert, midface and intermediate) indicated that the ratios between the pore pressures at each of the locations remained essentially constant throughout the dissipation and rotation phases with $\Delta u_{inv} > \Delta u_{int} > \Delta u_{mf}$.

Based on this observation, it is reasonable to deduce a model for β based on pore pressures in the LDFE simulations outlined in the companion paper (Schneider et al., 2019b). An advantage of using the LDFE dissipation simulations, compared to previously reported SSFE wished-in-place calculations, is that the potential effect of soil heave is captured appropriately, although Schneider et al. (2019b) found that soil heave around the periphery of the penetrometers has minimal influence on the dissipation characteristics. More information regarding the modelling procedure (the RITSS technique after Hu & Randolph, 1998), the model geometry and adopted Modified Cam Clay parameters can be found in the companion paper.

Figure 3a illustrates the dependency of the β-factor on the transducer location (denoted here by the angle θ, according to Figure 1) and normalised embedment for a rough hemiball under normally consolidated soil conditions. An effective non-dimensional embedment depth, w'/D, which accounts for the change of contact area around the penetrometer induced by soil heave, was introduced to link the numerically derived results to their corresponding embedment. The scaling factor remains practically constant as the excess pore water pressures dissipate, as demonstrated by the grey lines in the figure (which are effectively indistinguishable), where

each line corresponds to a different dissipation time. The dashed lines are best fits, each corresponding to a specific non-dimensional embedment, w'/D, taken as the mean of the initial and final post-consolidation values. The β-factors derived numerically at the invert position ($\theta = 0$) are in good general agreement with the values reported by Yan (2014).

A relationship was derived using a nested fitting technique (i.e. via definition of a main function composed of various sub-functions), to estimate how β varies with the transducer location, θ, and the effective embedment depth, leading to

$$\beta = \frac{\Delta u_{ave}}{\Delta u_{pos}} \approx \min\left(\frac{1}{a + b\ \theta^{c}}, 1.5\right) \qquad where \qquad 0.1 \le w'/D \le 0.5 \tag{11}$$

with θ expressed in radians.

The coefficients a, b and c can be defined using the following polynomial equations:

$$a = p_1 (w'/D)^2 + p_2 (w'/D) + p_3 \tag{12}$$

$$b = 1 \Big/ \left(p_4 (w'/D)^2 + p_5 (w'/D) + p_6 \right) \tag{13}$$

$$c = p_7 (w'/D)^2 + p_8 (w'/D) + p_9 \tag{14}$$

with the constants p_1-p_9 given in Table 1. The resulting model was verified through additional LDFE simulations, as shown in Figure 3b for the invert, intermediate and midface positions. The LDFE results also show that the scaling factor relationship developed appears reasonably consistent across the *OCR* range of 1-6, which covers the range of practical interest for deep water offshore conditions.

Table 1: Coefficients for approximation of the scaling factor β

Coefficient *a*		Coefficient *b*		Coefficient *c*	
p_1	$-2.62 \cdot 10^{-2}$	p_4	2.68	p_7	1.87
p_2	$3.03 \cdot 10^{-1}$	p_5	-4.7	p_8	-1.58
p_3	1.32	p_6	$7.76 \cdot 10^{-2}$	p_9	2.31

For back-analysis of the laboratory tests, the initial excess pore pressures were adjusted after Sully et al. (1999) to account for the slight delay in measurement of the dissipation response at the start of the rotation phase. Equation (11) was used to define the scaling factor, β, for the hemiball. For the toroid, a value of 0.725 was determined (Schneider et al., 2019a), which is in agreement with numerical SSFE solutions reported by Yan (2014). This value is similar to that derived for the hemiball invert location (Figure 3a).

TEST VARIATIONS FOR THE ROTATION STAGE

Details regarding the penetration (undrained penetration to w/D = 0.3) and load-controlled dissipation stages can be found in the companion paper (Schneider et al., 2019b). The next sections present results from the rotation stage for both the hemiball and toroid penetrometer. Three potential types of rotation stage were defined and investigated: the basic rotation test (BT), the episodic rotation test (ERT) and the over-consolidation test (OCT), with each test variation targeting a different set of soil properties, as outlined in Table 2. A brief overview of the testing programme, together with a summary of the inferred soil properties from each test, is given in Table 3.

Table 2: Variations in test protocol for the rotation stage.

Variant	**Characteristics of rotation stage**	**Measurements**	**Targeted properties**
BT	*fms*-rotation *(fast, medium, slow)*	T, Δu, w (*LC: V=constant*) *	$(s_{u,int}/\sigma'_{no})_{nc}$, δ
ERT	cycles of fast rotation & dissipation		$(s_{u,int}/\sigma'_{no})_{nc}$, δ, κ/λ
OCT	rotation at different OC-ratios		m , $\delta = f(\sigma'_n)$

* Vertical load corresponds to maximal penetration resistance at final embedment (BT & ERT) or a specific fraction of it (OCT)

An undrained penetration (stage 1) followed by a load-controlled (abbreviated herein as LC) dissipation phase (stage 2) were carried out prior to all test variations summarised in Table 2 (stage 3). The same vertical load, as achieved at the end of the penetration phase and maintained throughout the dissipation phase (stage 2), was maintained for the entire rotation phase in the BT and ERT tests. The vertical load was adjusted systematically in the OCT tests after the dissipation stage to achieve the targeted over-consolidation ratios for the soil (stage 3). The penetration phase involved monotonic penetration with no remoulding cycles, so as to limit device settlements during rotation)

RESULTS: BASIC ROTATION TEST (BT)

To define the whole backbone curve it is necessary to rotate for a normalised time $T_{rot} = c_v t/D^2 \sim 1$ to reach the drained limit (the coefficients of consolidation, c_v, corresponding to the invert of the penetrometer and estimated from the preceding dissipation phase (Schneider et al., 2019b) were used to define non-dimensional time T_{rot}). It is also necessary to rotate by a sufficient distance to reach sliding failure prior to pore pressure dissipation, in order that the undrained interface strength can be identified before consolidation occurs. Toroid experiments published by Schneider et al. (2019a) showed that a non-dimensional circumferential displacement, dx/D (at the effective radius r_{eff}), of about 0.02 is required for failure. The time for significant (e.g. 10%) drainage is $T_{rot} \sim 0.001$ (Yan et al., 2014). A rotation of several revolutions would therefore be required before drained conditions are reached, which would

create excessive settlement and cause the penetrometer to move into fresh soil, generating further excess pore pressure. A practical solution is to begin with a rotational speed sufficient to identify the undrained strength prior to consolidation occurring, and then reduce the rotation speed in steps to limit the total rotation and eliminate excessive settlements. Experience gained in the laboratory from several tests indicated that a reduction in rate of about one order of magnitude, from one sub-stage to the next, leads to reasonable results. This allows the 'full' backbone curve to be measured whilst generating relatively modest device settlements during rotation. For example, in this study those settlements were ~20 mm (w/D ~0.8) and ~25 mm (w/D = 0.25) for the toroid and hemiball, respectively (see also Figure 5e).

Using this approach, the basic or BT test constitutes three consecutive rotation sub-stages with fast, medium and slow rotation rates (relative to each other). Initially, the penetrometer is rotated at a fast rate (e.g. toroid: rotation rate ω of ~0.004 radians/s to give $V_{rot} = \omega r_{eff} D/c_v \geq$ ~10) to characterise the undrained part of the backbone curve. In the subsequent rotation sub-stages the rotation rate is reduced in order to measure the remainder of the backbone curve without inducing excessive settlement. These changes in rotation rates lead to an abrupt but temporary drop in torque (see Figure 2). Figure 4 shows a schematic of the basic elements of such a test in terms of accumulated vertical displacement and rotation angle.

Experimental results of three toroid and hemiball tests are shown in Figure 5 and Figure 6, interpreted using the total and effective stress interpretation frameworks, respectively. Each test comprised a fast, medium and slow rotation sub-stage (*fms*-rotation) with load-control held within ± ~1N (nominal contact stress: ± ~0.15 kPa) throughout, demonstrating high stability of the system. As mentioned before, reduction of the rotation speed leads to a sudden drop in the measured resistance (mobilised torque), as seen in Figure 5, which is perhaps due to the strain rate dependency of kaolin clay (e.g. Lehane et al., 2009). If the rate reduction is too severe, it is possible that the measured interface friction might not recover in time to successfully track the entire backbone curve, as occurred in the hemiball test 'Hemi_BT-1' in Figure 5c. Even

though it is not possible to define the complete total stress backbone curve from this particular test, the data can still be used to estimate the undrained and drained limits of the interface friction properties. Due to its smaller diameter, the toroid needs to be rotated significantly faster than the hemiball to ensure undrained conditions. This makes the load-control more challenging and results in slightly noisier data for the fast rotation sub-stage of the toroid tests (Figure 5a).

An excellent match of the measured rotation response was found for all toroid and hemiball tests, as illustrated in Figure 5. The undrained and drained limits, identified according to Figure 2, lead to a normally-consolidated interface strength ratio, $R = (s_{u,int}/\sigma'_{no})_{nc}$, of about ~0.15 and an interface friction angle, δ, of ~19-20º. This strength ratio is in close agreement with shear strength data for kaolin from geotechnical centrifuge tests (Hu et al., 2014; Morton et al., 2014), reflecting the rough nature of the interface. The inferred interface friction angle agrees well with the measurements of Chen & Randolph (2007).

The effect of the slight over-consolidation of the soil specimen, which is a function of the pre-consolidation stress of ~20 kPa and the final penetration resistance, V_{max}, maintained constant during the preceding dissipation stage, was taken into account according to Equation (8). The *OCR*-correction (*OCR* ~1.5-2) combined with a SHANSEP parameter of $m = 1 - \kappa/\lambda \approx 0.785$, which is an estimate based on the critical state parameters for kaolin clay (after Stewart, 1992: $\lambda = 0.205$, $\kappa = 0.044$), results in all of the responses in Figure 5 yielding very consistent undrained strength ratios of around ~0.15, as stated previously. A summary of all interpreted soil friction parameters can be found in Table 3.

Fitting backbone curves to the test measurements (dashed black lines) leads to experimentally derived values of $T_{rot,50}$ (time at which ~50% of excess pore pressures have dissipated) of ~0.018 and ~0.130 for the hemiball and toroid, respectively. The estimated values are consistent with the numerical SSFE simulation results reported by Yan (2014).

Figure 6 presents the effective stress interpretation of the same data, alongside the non-linear failure envelopes derived from the shear box tests. The stress path rises gradually from left to right as excess pore pressures dissipate with increasing test duration. All penetrometer tests are in excellent agreement with each other and are bracketed by the interface shear box data generated using the two low stress correction methods after Lehane & Liu (2013). The penetrometer measurements fall closer to the corrected interface shear box data corresponding to soil ingress between the two halves of the shear box (correction approach 2). Post-test disassembly of the interface shear box apparatus attested that such soil ingress did in fact occur.

RESULTS: EPISODIC ROTATION TEST (ERT)

Operational pipelines are subjected to regular cycles of heating and cooling during operation and shutdown periods. This causes the pipeline to expand and contract over relatively short timescales resulting in stress-reversals on the pipe-soil interface (Carr et al., 2006). The movement period is typically short enough to involve an undrained soil response, but the intervening period between movements is sufficiently long for consolidation to occur. This regime can be mimicked by performing episodic rotation tests with repeated fast rotation phases (modelling the transition between shutdown and operational states) and intervening consolidation periods. The intervening consolidation phases, following each fast rotation phase ($V_{rot} \geq$ ~10), should be sufficiently long to allow most of the generated excess pore pressures to dissipate (e.g. ~90% of consolidation complete). It was important to minimise the angle of rotation to avoid excessive settlements, while ensuring sufficient rotation to mobilise the full undrained resistance in each episode. Figure 7 shows a schematic of the basic elements of such a test in terms of accumulated vertical displacement and rotation angle.

Yan et al. (2014) quantified the episodic transition from undrained to drained sliding response using a drainage index, ψ, expressed as

$$\psi = 1 - \exp\left[-0.7 \cdot (N-1)/(N_{50}-1)\right] \qquad with \qquad N_{50} = \frac{0.9}{(\kappa/\lambda)} \tag{15}$$

where N is the cycle number and κ/λ is the elastic-plastic volumetric stiffness ratio. N_{50} represents the testing cycle corresponding to ~50% hardening and consequently a drainage index of ~0.5. The relationship was derived from numerical simulations modelling pipelines on normally consolidated soil, but can equally be used to back-analyse ERT tests. An alternative expression, based on a simplified critical state interpretation of the stress:voids ratio path during episodes of sliding and reconsolidation (White et al., 2015b) is

$$\psi = \frac{(R_c)^a - 1}{R_c - 1} \qquad with \qquad a = 1 - \left(1 - \frac{\kappa}{\lambda}\right)^{N-1} \tag{16}$$

where the episodic strength increase is controlled by the stiffness ratio κ/λ and the critical state spacing ratio R_c between the isotropic consolidation and critical state lines (with R_c = 2 for the Modified Cam Clay soil model).

An episodic test allows N_{50} to be derived directly, which has practical value in indicating the number of operational cycles required for the seabed friction to rise towards the drained limit. Equations (15) and (16) allow N_{50} to be estimated from κ/λ or vice versa, which facilitates linking of N_{50} to laboratory measurements of soil stiffness.

Results of three episodic rotation tests are presented in Figure 8, with all the tests comprising 20 fast rotation and consolidation cycles, which is adequate to reach drained conditions (Yan et al., 2014).

The ultimate undrained resistance rises gradually, as the soil hardens from episode to episode, as indicated in Figure 8b. Total stress interpretation of the tests yields almost identical soil friction properties as derived with the basic rotation tests (Table 3). When plotted in effective stress space, most of the data points, with each corresponding to a different rotation cycle, lay

within the relatively close bounds of the two shear box interpretation methods described earlier in the paper (Figure 8c).

Figure 9 shows the rise in drainage index, ψ, with increasing cycle number, N. The stiffness ratio, κ/λ, derived when fitting the theoretical model of Yan et al. (2014) to the test measurements, is estimated to be about ~0.155 (mean value from all tests), with the relationship proposed by White et al. (2015b) yielding a very similar value (Figure 9). The best fit values determined for each test using Equation (15) are stated in Table 3 and are consistent with the parameters quoted by Stewart (1992). The cycle number corresponding to ~50% hardening, N_{50}, is found to be similar for both penetrometers, with about 6 cycles required to reach a drainage index of 0.5.

RESULTS: OVER-CONSOLIDATED TEST (OCT)

Submarine pipelines are typically filled with water after laying, to improve stability and to assist in system testing. During operation they transport hydrocarbons with a lower density than seawater, which creates local over-consolidation in the underlying soil mass. Depending on the pipeline diameter and the history of contents (e.g. oil or gas, and whether the pipeline was water-filled prior to operation), the conditions of interest are generally encompassed by an OCR in the range of 1-8 (Low et al. 2017). To measure the response of soil for this situation, the vertical load held on the shallow penetrometers was varied towards the end of the dissipation stage and prior to the initial rotation stage (or at the end of the preceding rotation stage), as follows:

- Sub-stage 1: Unloading to V_{max} / 4 followed by dissipation & rotation phase
- Sub-stage 2: Reloading to V_{max} / 2 followed by dissipation & rotation phase
- Sub-stage 3: Reloading to V_{max} followed by dissipation & rotation phase

Figure 10 illustrates the OCT methodology in terms of penetrometer embedment, vertical load and rotation angle. For clarity only one sub-stage is presented. Any stress level dependency of the friction angle, $\phi' = f(\sigma'_n)$, as is often reported at low effective stresses (e.g. White et al., 2012), can be determined with this type of test. Additionally, the SHANSEP exponent, *m*, can be evaluated for the case where the undrained stress ratio, $(s_{u,int}/\sigma'_{no})_{nc}$, is known from an alternative penetrometer test (e.g. BT or ERT). Another possibility to assess the SHANSEP parameter is to estimate the normally consolidated stress ratio by including an undrained *OCR* = 1 sub-stage into the testing routine, as in sub-stage 3 defined above earlier (noting that any shear induced change in water content due to the previous rotation sub-stage(s) is not accounted for and thus the nominal over-consolidation ratio stated for sub-stages 2 and 3 will be a slight underestimation of the true *OCR* present in reality).

Figure 11 shows a toroid test with two sub-stages, with each consisting of an *fms*-rotation phase and each corresponding to a different over-consolidation ratio. The penetrometer is rotated while maintaining either a quarter (first stage) or half (second stage) of the final penetration resistance achieved at the end of the penetration stage. Again, adopting a pre-consolidation stress of 20 kPa and assuming practically complete consolidation around the penetrometer, such loading conditions result in over-consolidation ratios of *OCR* ~6.4 and *OCR* ~2.9 for the first and second sub-stage, respectively. To provide reference, two basic tests are plotted alongside the OCT-test results in Figure 11.

Due to the high over-consolidation ratio, a high undrained peak in friction was recorded during the first sub-stage. With increasing shear displacement the normalised axial friction eventually drops to a residual value of about ~0.8. Drained conditions were reached at a normalised time of about T_{rot} ~1 for both stages. Stress level dependency of the friction angle, as often observed at very low effective stresses (e.g. White et al., 2012; White et al., 2015a), can be seen clearly in Figure 11b, with the interface friction angle decreasing from ~27.8 to 23.1 degrees from the first to the second sub-stage (reference value corresponding to BT tests: δ ~19-20º). The

SHANSEP exponent, *m*, was evaluated as ~0.84 (exact values, see Table 3), assuming an undrained normally-consolidated strength ratio according to the basic tests described previously. The inferred exponent is in excellent agreement with the results obtained from the episodic rotation tests.

In effective stress space, the measurements obtained for the different over-consolidation ratios are all consistent with each other, falling between the bounds given by the two shear box correction approaches (Figure 11c). However, the stress path corresponding to the *V*/4-test (first sub-stage) moves in the opposite direction to the *V*/2-test (second sub-stage). This is due to the generation of negative excess pore pressures during the undrained rotation of the device, which generated a large peak resistance in the total stress interpretation. Similar observations were also reported by Martinez & Stutz (2018) for interface shear box tests on over-consolidated clay samples. This is compelling evidence of the reliability of the effective stress interpretation framework.

Due to time constraints (for example during offshore in-situ testing) it is often not practical to fit several *OCR* sub-stages into one test, as this may lead to test durations as long as several days for slow-draining fine-grained soils. Figure 12 shows the results of two hemiball OCT-tests, with each consisting of only one *fms*-rotation sub-stage, corresponding to an *OCR* of approximately ~6.5 (*V*/4). The test measurements are in excellent agreement with each other, both in total and effective stress space. The inferred SHANSEP parameter is *m* ~0.82, which is again consistent with existing literature (e.g. Stewart, 1992; Lehane et al., 2009) and the stiffness ratio estimated from the ERT-tests (note: $m \sim 1 - \kappa/\lambda$, according to Equation 8). The evaluated friction angles, $\delta \sim \phi'$, are 20.7 and 18.8 degrees for the two tests (Table 3). The observed stress level dependency of the interface friction is much smaller for the hemiball, and practically non-existent for the Hemi_OCT-2 test, which may be a consequence of reduced dilation for the axisymmetric conditions (e.g. Bolton, 1986) of the hemiball, compared to the

pseudo plain strain conditions of the toroid ($L/D = 2$). Again, in effective stress space, the stress path moves in the opposite direction, indicating negative excess pore pressures are created due to dilation, as shown in Figure 12c.

SUMMARY

The derived parameters are summarized in Table 3 (total stress interpretation). Mean values and coefficients of variation (COV) of each parameter are quoted at the bottom of the table to demonstrate the exceptional repeatability of the tests. The consistency of the measurements is remarkable, especially when compared to typical values of coefficients of variation characterizing the inherent state of soil (e.g. undrained shear strength: ~30-50% and angle of internal friction: ~5-15% after Schneider & Schneider, 2013). In effective stress space, all test types overlay the same failure envelope as can be seen in Figure 13a. The effective interface friction and the relatively narrow range of the resulting envelope parameters (adopting the stress dependent failure criterion of White & Randolph, 2007) are presented in Figure 13b.

Table 3: Summary of rotation tests and derived soil parameters (total stress interpretation)

Test name	$(s_{u,int}/\sigma'_{no})_{nc}$	$\tan\delta$	κ/λ *	m
	(-)	(-)	(-)	(-)
Toro_BT-1	0.158	0.342	—	—
Toro_BT-2	0.149	0.360	—	—
Toro_BT-3	0.144	0.345	—	—
Toro_ERT-1	0.145	0.346	0.145	—
Toro_ERT-2	0.165	0.340	0.170	—
Toro_OCT-1	—	0.527 / 0.427	—	0.845 / 0.843
Hemi_BT-1	0.146	0.335	—	—
Hemi_BT-2	0.150	0.339	—	—
Hemi_BT-3	0.155	0.338	—	—
Hemi_ERT-1	0.144	0.360	0.150	—
Hemi_OCT-1	—	0.378	—	0.820
Hemi_OCT-2	—	0.340	—	0.820
Mean	~0.151 [+]	~0.345 [+]	~0.155	~0.832
COV [#]	~5% [+]	~3% [+]	(~8%)	(~2%)

* Stiffness ratios κ/λ were derived using the back-analysis method of Yan et al. (2014) given by Equation 15.

[+] Only the basic rotation (BT) and episodic rotation tests (ER T) were used to define the statistical measure.

[#] Intended to demonstrate consistency only (not to be used to define distributions of interface / soil properties).

The data presented in this paper and its companion (Schneider et al., 2019b) has demonstrated that the hemiball and toroid shallow penetrometers are capable (when coupled with a miniature T-bar or ball penetrometer test) of measuring practically all of the parameters required by modern pipeline design guidelines (e.g. DNVGL-FP-F114) as summarised in Table 4. For example, for recent projects we have performed such a suite of tests directly in box core samples onboard a survey vessel within a few hours of the sample being recovered. A major advantage of these tests is that preliminarily interpreted data can be fed back to the client and pipeline design team earlier in the project cycle than for conventional tests, which typically need to be performed onshore in a laboratory.

Table 4: Investigated testing variations and definition of recommended standard set of tests

Testing phase	Soil parameter	BT [3]	ERT [3]	OCT	T-bar [3]
Undrained Penetration	s_u	✓	✓	✓	✓
	$s_{u,rem}$ & S_t				✓
Dissipation	c_v	✓	✓	✓	
Rotation (BT, ERT, OCT)	$\tau_{u,int}$	✓	✓	✓	
	$(s_{u,int}/\sigma'_{no})_{nc}$ & m [2]	$(s_{u,int}/\sigma'_{no})_{nc}$	$(s_{u,int}/\sigma'_{no})_{nc}$	✓	
	δ or ϕ'	✓	✓	✓	
	(κ/λ) & N_{50}		✓		
Penetration [1]	$s_{u,c}$	✓	✓	✓	(✓)

[1] Further penetration after complete consolidation / [2] SHANSEP parameters / [3] Testing component of standard set

CONCLUSIONS

Shallow penetrometer tests have been demonstrated to be capable of measuring undrained strength, consolidation and friction parameters of soft surficial soils within a single test. This paper has focused on the rotation stage, potential variations of it, and the interface / soil properties that can be derived reliably from them. Geotechnical relationships needed for data interpretation, both in terms of a total and an effective stress framework have been presented. New expressions for evaluating the pore pressure scaling factor of the hemiball, which is a key back-analysis parameter, are presented based on large deformation FE-simulations. Additionally, results from a wide-ranging set of laboratory tests in kaolin clay illustrate the proposed test protocols and back-analysis methods.

The main outcomes and future prospects for shallow torsional penetrometers can be summarised as follows:

- The laboratory tests have demonstrated that the hemiball and toroid can provide rapid and reliable assessment of key parameters for pipeline design in soft surficial soil. The inferred friction and stiffness associated parameters are very consistent with existing

literature and independent shear box measurements for the kaolin clay used in the investigation.

- Direct assessment of the failure envelopes in effective stress space has been demonstrated via comparison of the interpreted measurements with data from low stress interface shear box tests.
- The results clearly show that comprehensive soil characterisation is possible with the three test variations (BT, ERT and OCT) described. Coupled with complementary miniature T-bar or ball penetrometer tests, this suite of tests performed in a box core sample in-situ on the deck of a survey vessel would provide practically all of the pipeline design parameters required by recommended practices such as DNVGL-FP-F114.

This technology is now entering practice, and the tools and methodologies described above have been applied to several offshore projects.

ACKNOWLEDGEMENTS

The research presented here forms part of the activities of the Centre for Offshore Foundation Systems (COFS), currently supported as a node of the Australian Research Council Centre of Excellence for Geotechnical Science and Engineering (CE110001009). The first author is grateful for the support provided by an International Postgraduate Research Scholarship (IPRS) from the Australian Government. The second author was supported by an ARC DECRA Fellowship (DE170100119). Additionally, the work was supported by the Remote Intelligent Geotechnical Surveys (RIGSS) Joint Industry Project, with the participants Benthic Geotech, Fugro, Shell, Total and Woodside.

NOTATION

A,B	fitting parameters (effective stress failure criterion)
A_c	surface contact area
a,b,c	coefficients for approximation of β
c_v	coefficient of consolidation
D	device diameter
dx	shear displacement
L	lever arm (toroid penetrometer)
m	SHANSEP parameter
N	cycle number (episodic rotation routine)
N_{50}	cycle number corresponding to ~50% hardening
n	fitting parameter (backbone curve)
OCR	over-consolidation ratio
p_{atm}	atmospheric pressure
p_i	coefficients for approximation of β (p_1 - p_9)
R	normally consolidated strength ratio
R_c	critical state spacing ratio
r_{eff}	effective radius
S_t	soil sensitivity
s_u	undrained shear strength
$s_{u,c}$	consolidated undrained shear strength
$s_{u,int}$	undrained shear strength at penetrometer interface
$s_{u,rem}$	remoulded undrained shear strength
T	mobilised torque
T_{rot}	dimensionless rotation time
$T_{rot,50}$	dimensionless time, ~50% of excess pore pressures dissipated
t	time
u	pore water pressure
V	applied vertical load
V_{max}	vertical penetration resistance (end of penetration stage)
V_{rot}	dimensionless velocity (rotation stage)
v_{rot}	velocity during rotation stage
w	embedment depth
w'	effective embedment depth
α	rotation angle
β	scaling factor regarding excess pore pressure
Δu	excess pore water pressure
Δu_{ave}	average excess pore water pressure
Δu_{pos}	excess pore pressure at specific transducer location
δ	drained interface friction angle
ζ	wedging factor
θ	local inclination relative to vertical
θ_m	semi-angle of embedded segment

κ	slope of elastic compression line
λ	slope of virgin compression line
μ	interface friction coefficient
μ'	effective interface friction coefficient
μ_{dr}	drained friction ratio
μ_u	undrained friction ratio
σ'_n	effective normal contact stress
σ'_{no}	effective normal stress (at the start of the rotation phase)
$\sigma_{n,ave}$	averaged normal stress at penetrometer interface
$\sigma'_{n,ave}$	averaged effective normal stress at penetrometer interface
τ_{ave}	average shear stress at penetrometer interface
$\tau_{u,int}$	undrained interface friction
ϕ'	angle of internal friction
ψ	drainage index
ω	angular velocity

REFERENCES

Ballard J.-C., de Brier C., Stassen K. and Jewell R. (2013). Observations of pipe-soil response from in-situ measurements. Offshore Technology Conference, Houston, USA. Paper OTC 24154, 1-17.

Bolton, M. D. (1986). The strength and dilatancy of sands. *Géotechnique* **36**, No. 1, 65-78.

Carr, M., Sinclair, F. & Bruton, D. (2006). Pipeline walking – understanding the field layout challenges, and analytical solutions developed for the SAFEBUCK JIP. *Proc. Offshore Technology Conference*, Houston, OTC Paper 17945, 1-11.

Chen, W. & Randolph, M. F. (2007). External radial stress changes and axial capacity for suction caissons in soft clay. *Géotechnique* **57**, No. 6, 499-511.

Clayton, C. R. I., Siddique, A. & Hopper, R. J. (1998). Effects of sampler design on tube sampling disturbance – numerical and analytical investigations. *Géotechnique* **48**, No. 6, 847-867.

Det Norsek Veritas. (2017). DNVGL-RP-F114 - Pipe-soil interaction for submarine pipelines.

Hover, E. D., Ni, Q. & Guymer, I. (2013). Investigation of centreline strain path during tube penetration using transparent soil and particle image velocimetry. *Géotechnique Letters* **3**, No. 2, 37-41.

Hu, Y. & Randolph, M. F. (1998). A practical numerical approach for large deformation problems in soil. *International Journal of Numerical and Analytical Methods in Geomechanics* **22**, No. 5, 327-350.

Hu, P., Stanier, S. A., Cassidy, M. J. & Wang, D. (2014). Predicting peak resistance of spudcan penetrating sand overlaying clay. *J. Geotech. Geoenviron. Engng ASCE* **140**, No. 2, 04013009, 1-12.

Ladd, C. C., Foott, R., Ishihara, K., Schlosser, F. & Poulos, H. G. (1977). Stress-deformation and strength characteristics: state of the art report. *Proc. 9th Int. Conf. Soil Mech., Tokyo* **2**, 421-494.

Lehane, B. M., O'Loughlin, C. D., Gaudin, C. & Randolph, M. F. (2009). Rate effects on penetrometer resistance in kaolin. *Géotechnique* **59**, No. 1, 41-52.

Lehane, B. M. & Liu, Q. B. (2013). Measurement of shearing characteristics of granular materials at low stress levels in a shear box. *Geotechnical and Geological Engineering*, No. 31, 329-336.

Low, H.E., Ramm, M., Bransby, M.F., White, D.J. & Westgate, Z.W. (2017). Effect of through-life changes in soil strength and axial pipe-seabed resistance for HPHT pipeline design. Proc. Int. Conf. on Offshore Site Investigation and Geotechnics. SUT, London. 841-849.

Martinez, A. & Stutz, H. H. (2018). Rate effects on the interface shear behaviour of normally and overconsolidated clay. *Géotechnique*, ahead of print online, doi.org/10.1680/jgeot.17.P.311.

Meyer, V. M., Dyvik, R. & White, D. J. (2015). Direct shear interface tests for pipe-soil interaction assessment. *Frontiers in Offshore Geotechnics III – Meyer (Ed.)*, 423-428.

Morton, J. P., O'Loughlin, C. D. & White, D. J. (2014). Strength assessment during shallow penetration of a sphere in clay. *Géotechnique Letters* **4**, 262-266.

Randolph, M. F., White, D. J. & Yan, Y. (2012). Modelling the axial soil resistance on deep-water pipelines. *Géotechnique* **62**, No. 9, 837-846.

Schneider, H. R. & Schneider, M. A. (2013). Dealing with uncertainties in EC7 with emphasis on determination of characteristic soil properties. In *Modern Geotechnical Design Codes of Practice*, IOS Press, Amsterdam, the Netherlands, 87-101.

Schneider, M. A., Stanier, S. A., White, D. J. & Randolph, M. F. (2019a). Apparatus for measuring pipe-soil interaction behaviour using shallow 'pipe-like' penetrometers. *Submitted to Geotechnical Testing Journal*.

Schneider, M. A., Stanier, S. A., White, D. J. & Randolph, M. F. (2019b). Shallow penetrometers – Theoretical and experimental modelling of penetration and dissipation stages. *Accepted for publication by Canadian Geotechnical Journal*.

Stanier, S. A. & White, D. J. (2014). Shallow penetrometer penetration resistance. *Journal of Geotechnical and Geoenvironmental Engineering* **141**, No. 3, 04014117, 1-12.

Stewart, D. P. (1992). Lateral loading of piled bridge abutments due to embankment construction. PhD thesis, University of Western Australia.

Sully, J. P., Robertson, P. K., Campanella, R. G. & Woeller, D. J. (1999). An approach to evaluation of field CPTU dissipation data in overconsolidated fine-grained soils. *Canadian Geotechnical Journal* **36**, No. 2, 369-381.

Westgate Z. J., White D. J. & Savazzi M. (2018). Experience with interface shear box testing for axial pipe-soil interaction assessment on soft clay. *Proc. Offshore Technology Conference,* Paper OTC-28671-MS, 1-24.

White, D. J., Campbell, M. E., Boylan, N. P. & Bransby, M. F. (2012). A new framework for axial pipe-soil interaction, illustrated by shear box tests on carbonate soils. *Proc. 8th Intl. Conf. on Offshore Site Investigation and Geotechnics.* London: Society for Underwater Technology, 379-387.

White, D. J. & Randolph, M. F. (2007). Seabed characterisation and models for pipeline-soil interaction. *International Journal of Offshore and Polar Engineering* **17**, No. 3, 193-204.

White, D. J., Hill, A. J., Westgate, Z. J. & Ballard, J-C. (2010a). Observations of pipe-soil response from the first deep water deployment of the SMARTPIPE. *Frontiers in Offshore Geotechnics II – Gourvenec & White (eds),* 851-856.

White, D. J., Gaudin, C., Boylan, N. & Zhou, H. (2010b). Interpretation of T-bar penetrometer tests at shallow embedment and in very soft soils. *Canadian Geotechnical Journal* **47**, No. 2, 218-229.

White, D. J., Westgate, Z. J., Ballard, J-C., de Brier, C. & Bransby, M. F. (2015a). Best practice geotechnical characterization and pipe-soil interaction analysis for HPHT pipeline design. *Proc. Offshore Technology Conference,* Houston, OTC-26026-MS, 1-24.

White D. J., Leckie, S. H. F., Draper, S. & Zakarian, E. (2015b). Temporal changes in pipeline-seabed condition and their effect on operating behaviour. *Proc. Int. Conf. Offshore Mech. and Arctic Engng.* OMAE2015-42216, 1-10.

Wroth, C. P. (1984). The interpretation of in situ soil tests. *Géotechnique* **34**, No. 4, 449-489.

Yan, Y., White, D. J. & Randolph, M. F. (2011). Penetration resistance and stiffness factors for hemispherical and toroidal penetrometers in uniform clay. *International Journal of Geomechanics* **11**, No. 4, 263-275.

Yan, Y., White, D. J. & Randolph, M. F. (2014). Cyclic consolidation and axial friction for seabed pipelines. *Géotechnique Letters*, No. 4, 165-169.

Yan, Y. (2014). Novel methods for characterising pipe-soil interaction forces in-situ in deep water. PhD thesis, The University of Western Australia, Australia.

FIGURES

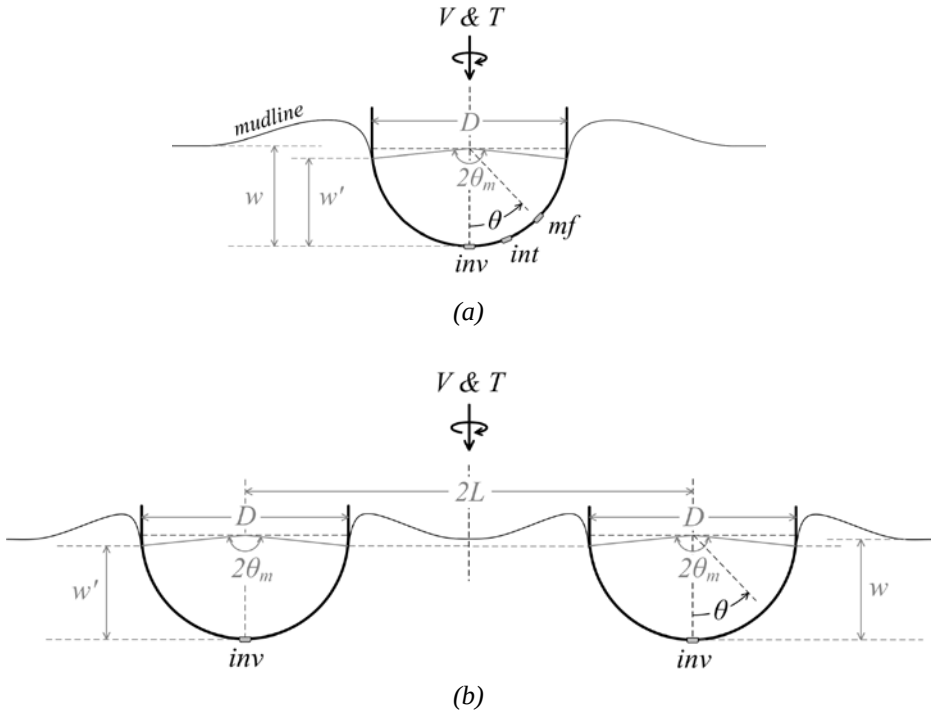

Figure 1: Device schematics and nomenclature after Schneider et al. (2019a): (a) hemiball; and (b) toroid.

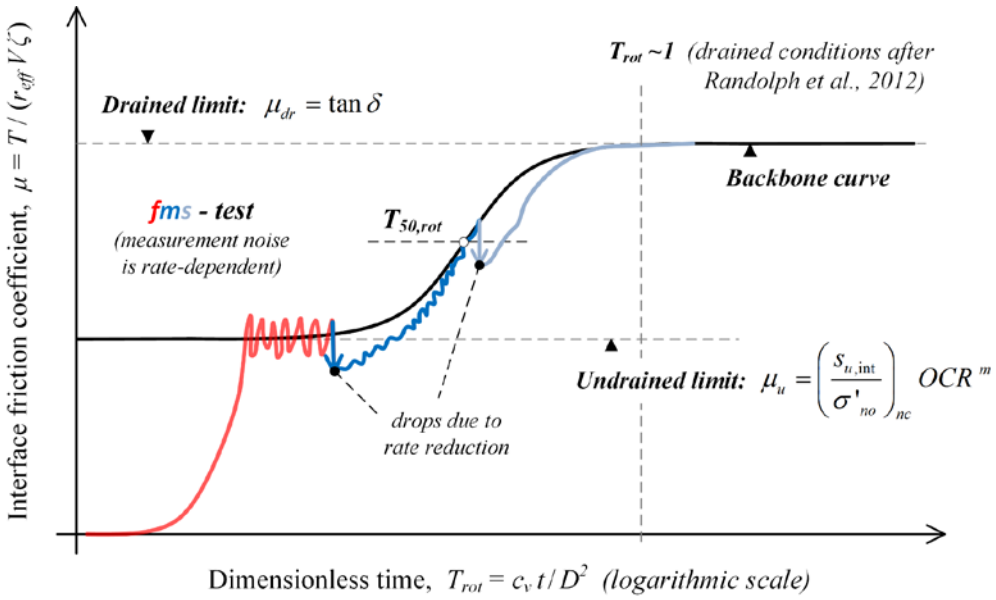

Figure 2: Illustration of total stress interpretation method for rotation stage.

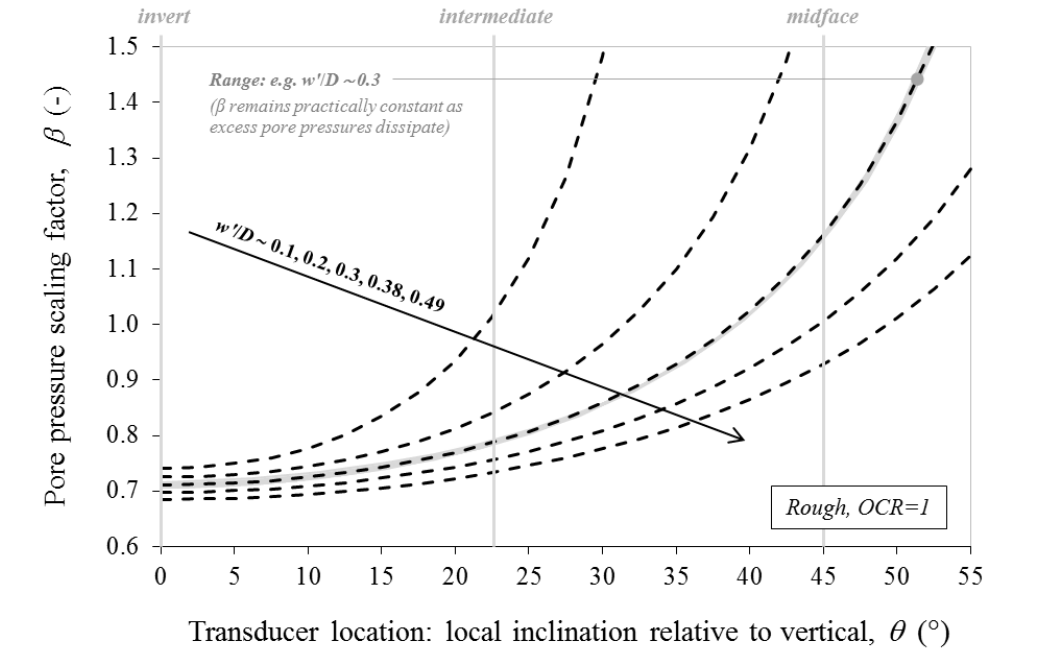

(a)

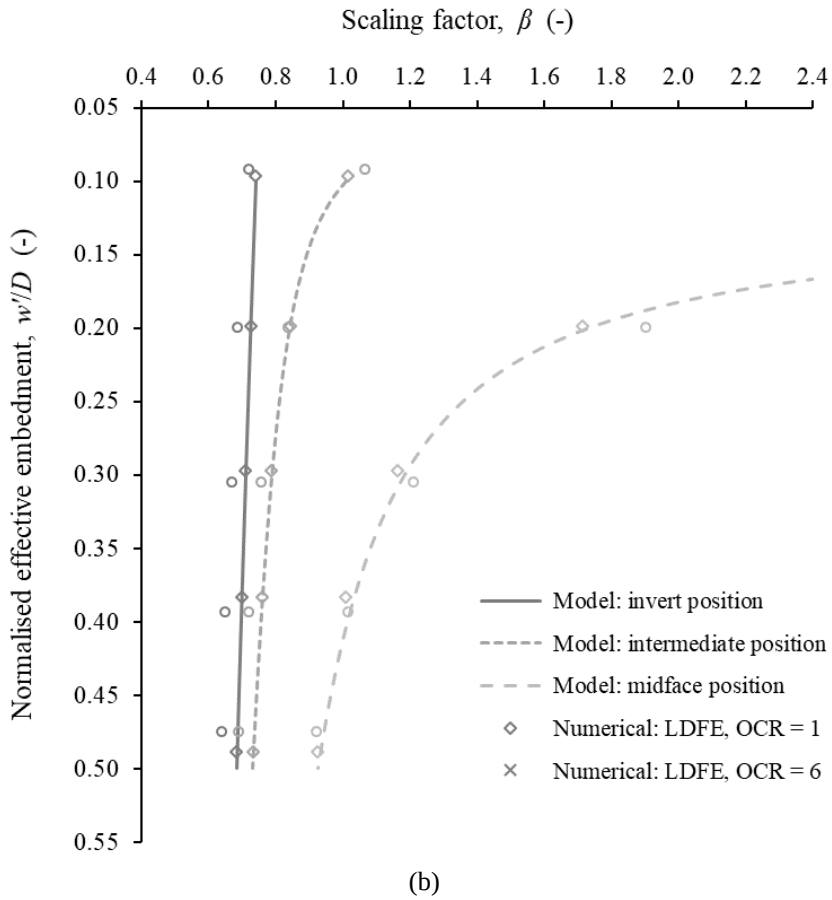

(b)

Figure 3: (a) Dependency of β-factor on local inclination, θ, and effective normalised embedment; and (b) performance of developed model compared with numerical LDFE-simulation results.

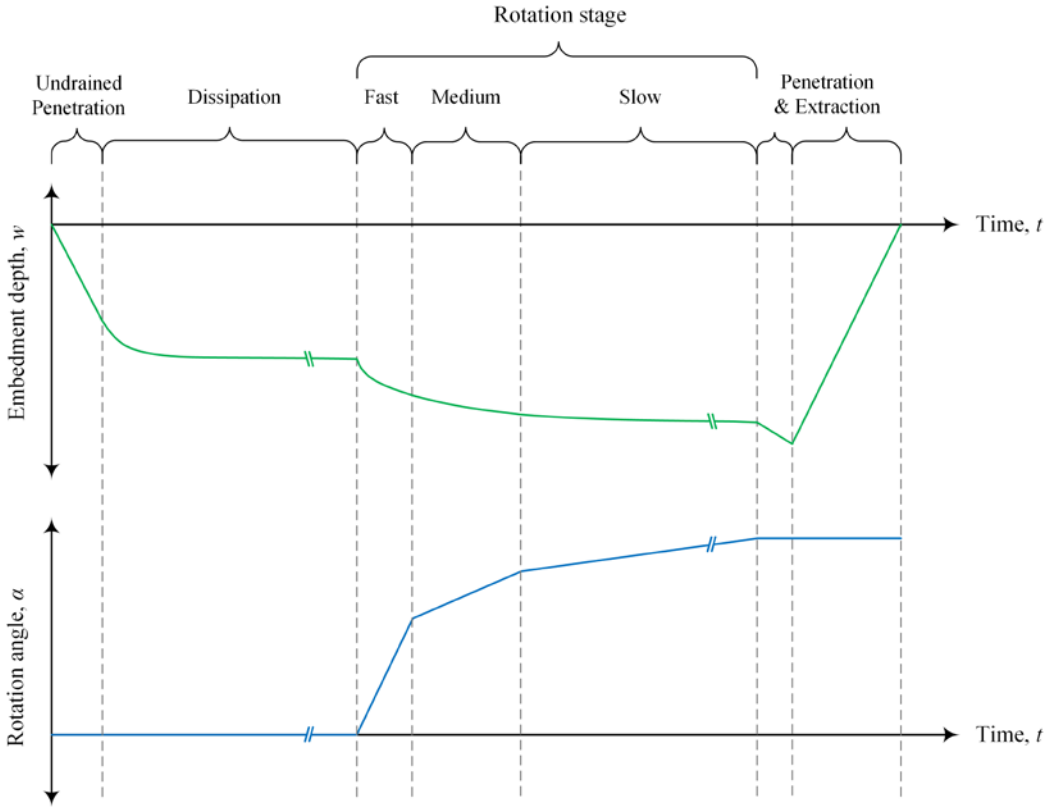

Figure 4: Basic rotation test after Schneider et al. (2019a): penetrometer embedment and rotation angle histories.

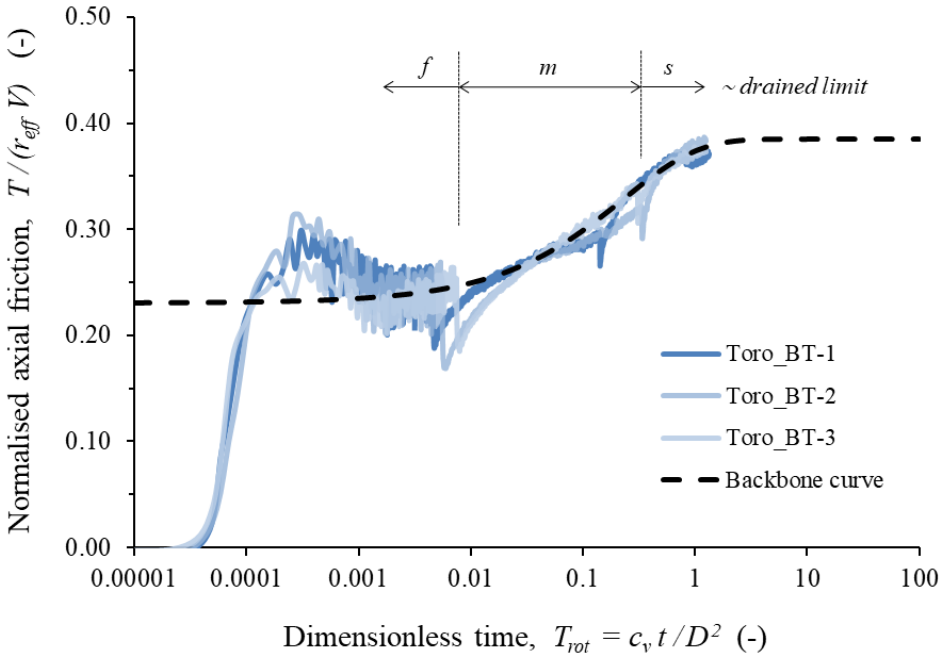
0.50
0.40
0.30
0.20
0.10
0.00
Normalised axial friction, $T/(r_{eff}V)$ (-)
f
m
s
~drained limit
Toro_BT-1
Toro_BT-2
Toro_BT-3
Backbone curve
0.00001
0.0001
0.001
0.01
0.1
1
10
100
Dimensionless time, $T_{rot} = c_v t/D^2$ (-)

(a)

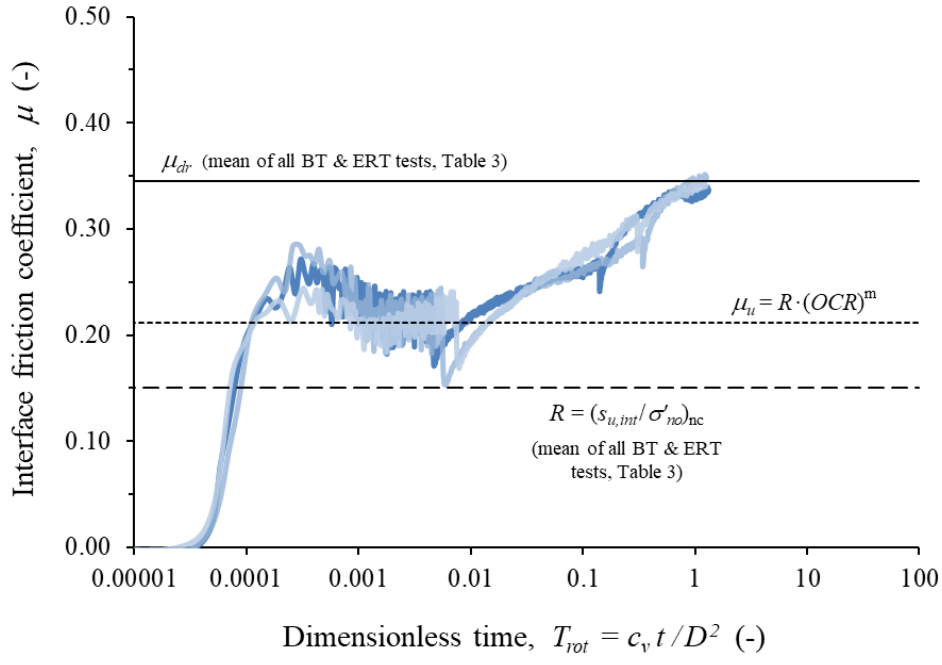
0.50
0.40
0.30
0.20
0.10
0.00
Interface friction coefficient, μ (-)
μ_{dr} (mean of all BT & ERT tests, Table 3)
$\mu_u = R \cdot (OCR)^m$
$R = (s_{u,int}/\sigma'_{no})_{nc}$
(mean of all BT & ERT tests, Table 3)
0.00001
0.0001
0.001
0.01
0.1
1
10
100
Dimensionless time, $T_{rot} = c_v t/D^2$ (-)

(b)

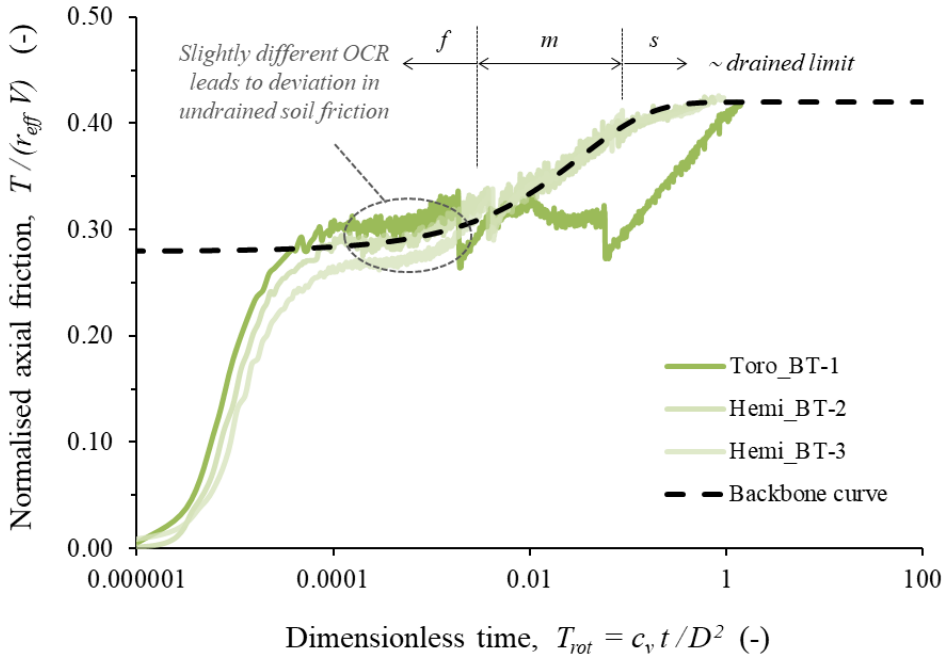
Slightly different OCR leads to deviation in undrained soil friction
f
m
s
~ drained limit
Toro_BT-1
Hemi_BT-2
Hemi_BT-3
Backbone curve
Normalised axial friction, $T/(r_{eff}V)$ (-)
0.50
0.40
0.30
0.20
0.10
0.00
0.000001
0.0001
0.01
1
100
Dimensionless time, $T_{rot} = c_v t/D^2$ (-)

(c)

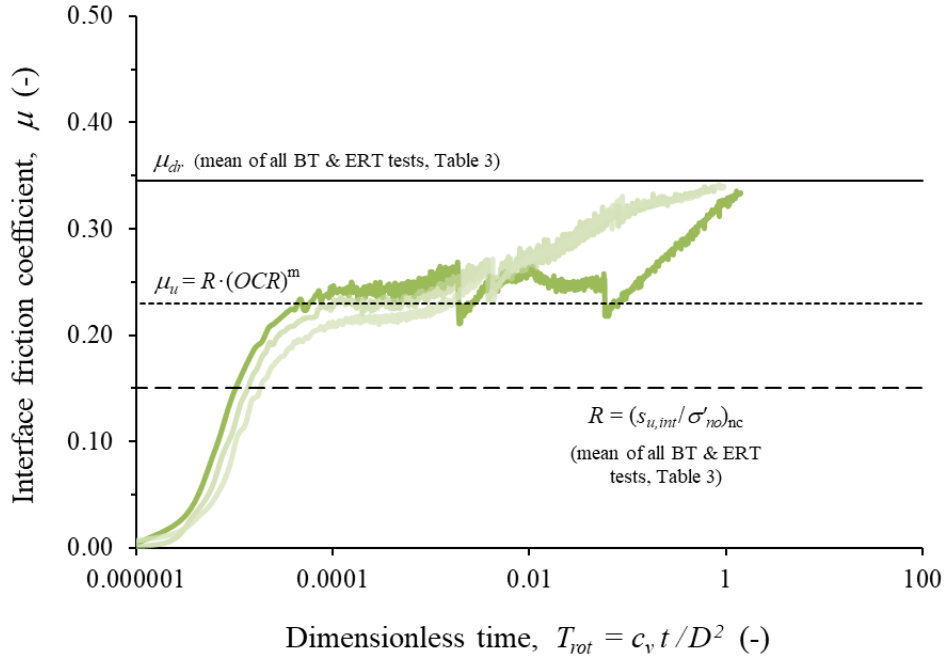
μ_{dr} (mean of all BT & ERT tests, Table 3)
$\mu_u = R \cdot (OCR)^m$
$R = (s_{u,int}/\sigma'_{no})_{nc}$
(mean of all BT & ERT tests, Table 3)
Interface friction coefficient, μ (-)
0.50
0.40
0.30
0.20
0.10
0.00
0.000001
0.0001
0.01
1
100
Dimensionless time, $T_{rot} = c_v t/D^2$ (-)

(d)

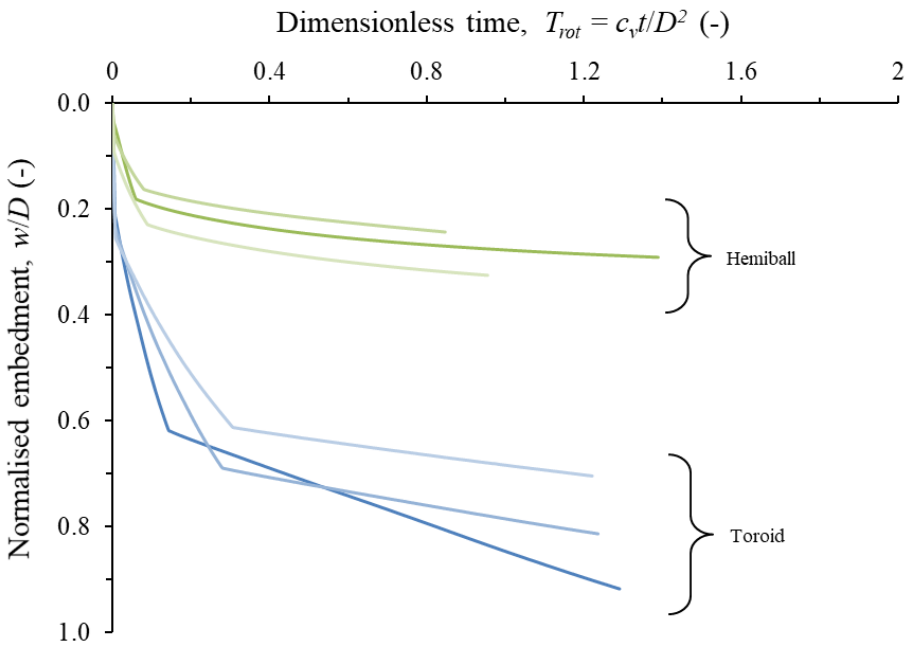

(e)

Figure 5: Total stress interpretation of basic *fms*-rotation test: (a, c) normalised axial friction; and (b, d) interface friction with dimensionless time for the toroid and hemiball, respectively; and (e) embedment depth with time for all tests presented.

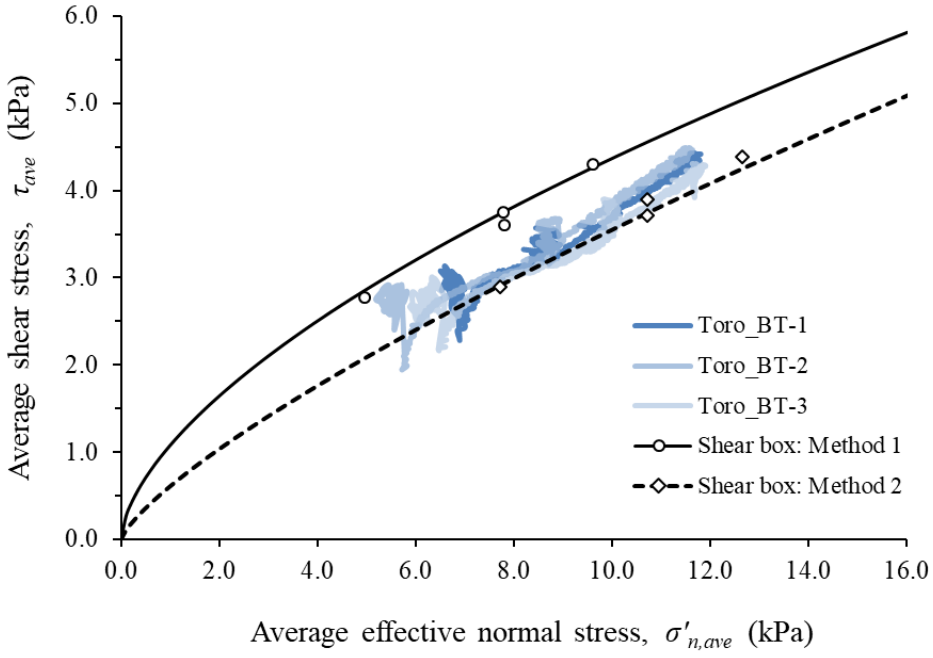

(a)

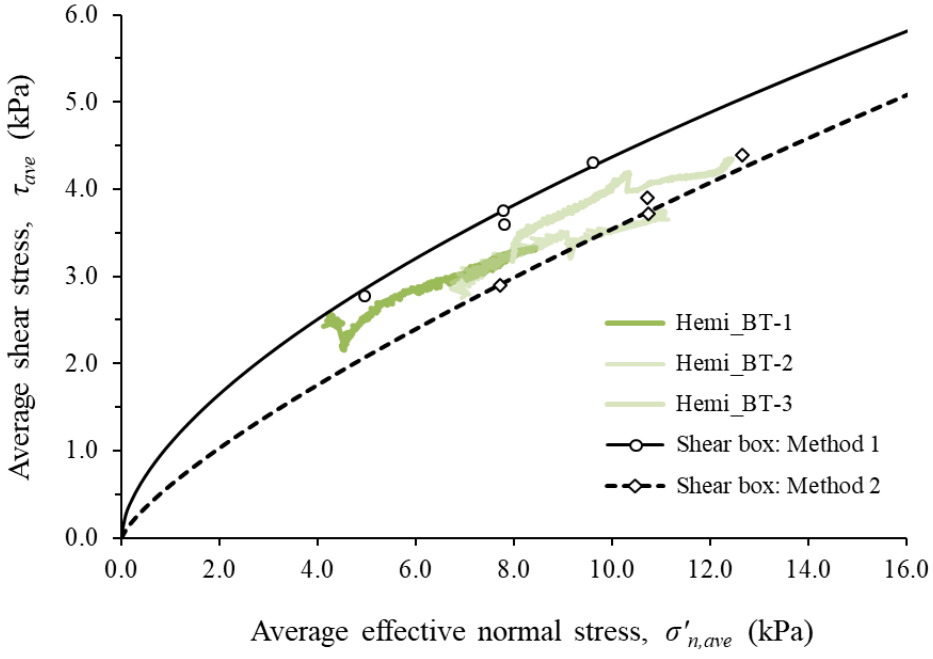

(b)

Figure 6: Effective stress interpretation of basic rotation test: (a) toroid; and (b) hemiball penetrometer.

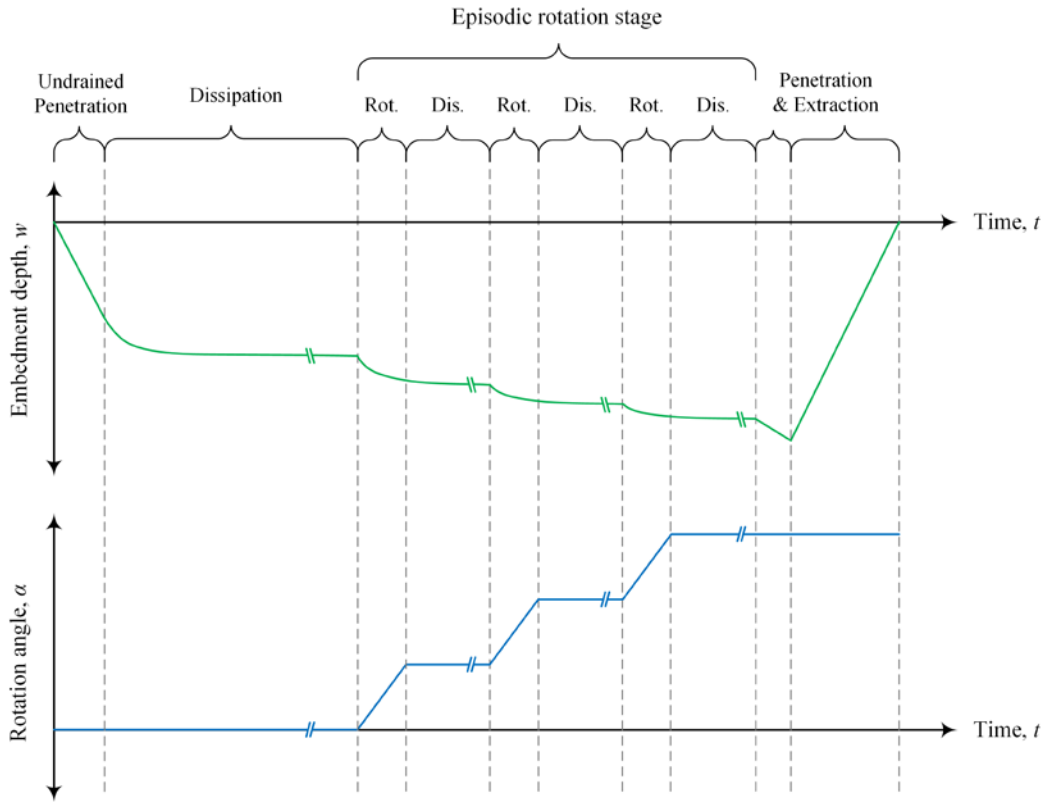

Figure 7: Episodic rotation test: penetrometer embedment and rotation angle histories.

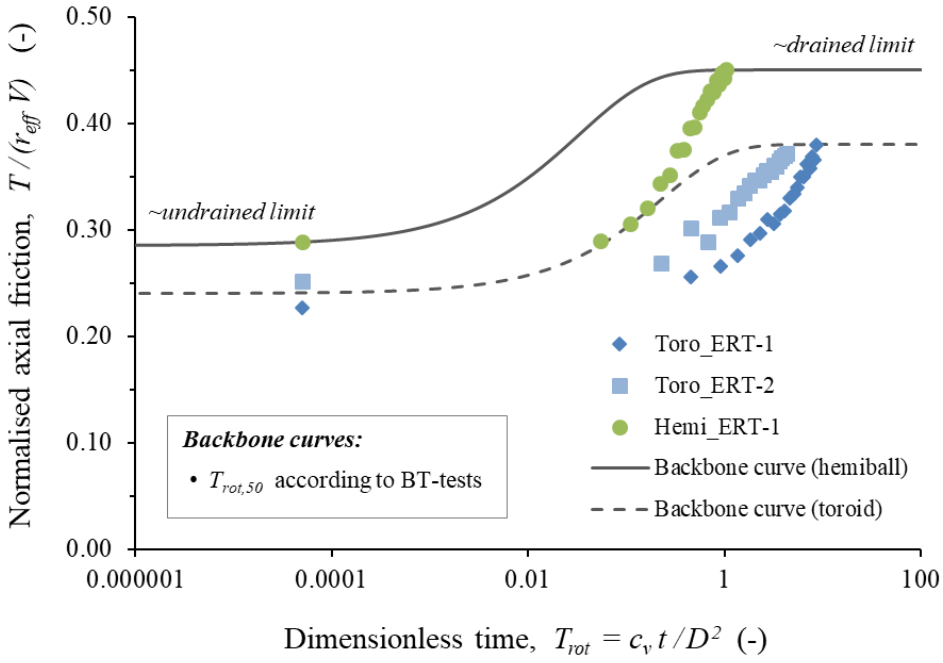
0.50
0.40
0.30
0.20
0.10
0.00
0.000001
0.0001
0.01
1
100
Normalised axial friction, $T/(r_{eff}V)$ (-)
Dimensionless time, $T_{rot} = c_v t/D^2$ (-)
~drained limit
~undrained limit
Toro_ERT-1
Toro_ERT-2
Hemi_ERT-1
Backbone curve (hemiball)
Backbone curve (toroid)
Backbone curves:
• $T_{rot,50}$ according to BT-tests

(a)

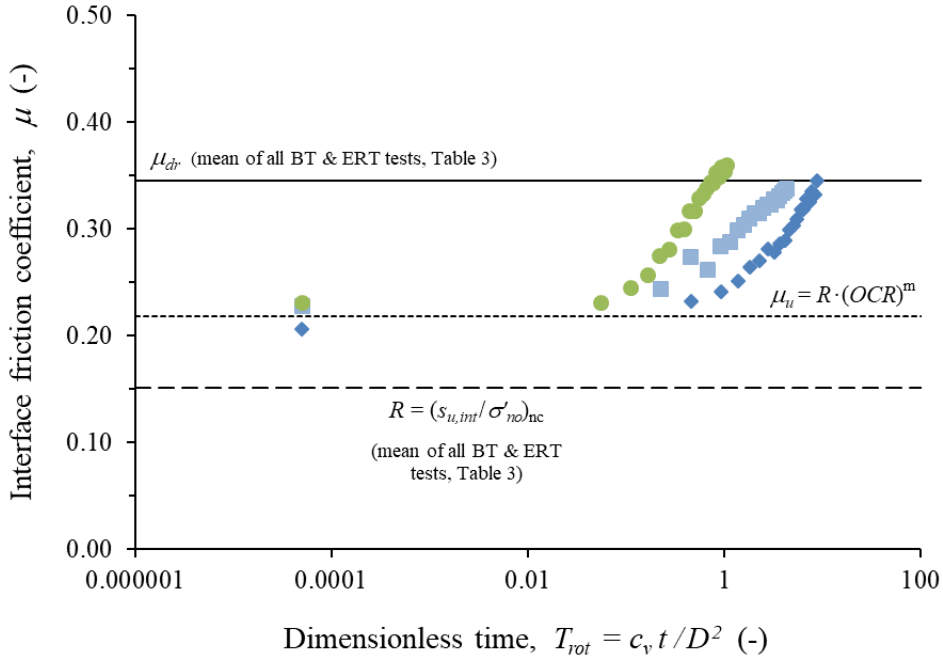
0.50
0.40
0.30
0.20
0.10
0.00
0.000001
0.0001
0.01
1
100
Interface friction coefficient, μ (-)
Dimensionless time, $T_{rot} = c_v t/D^2$ (-)
μ_{dr} (mean of all BT & ERT tests, Table 3)
$\mu_u = R \cdot (OCR)^m$
$R = (s_{u,int}/\sigma'_{no})_{nc}$
(mean of all BT & ERT tests, Table 3)

(b)

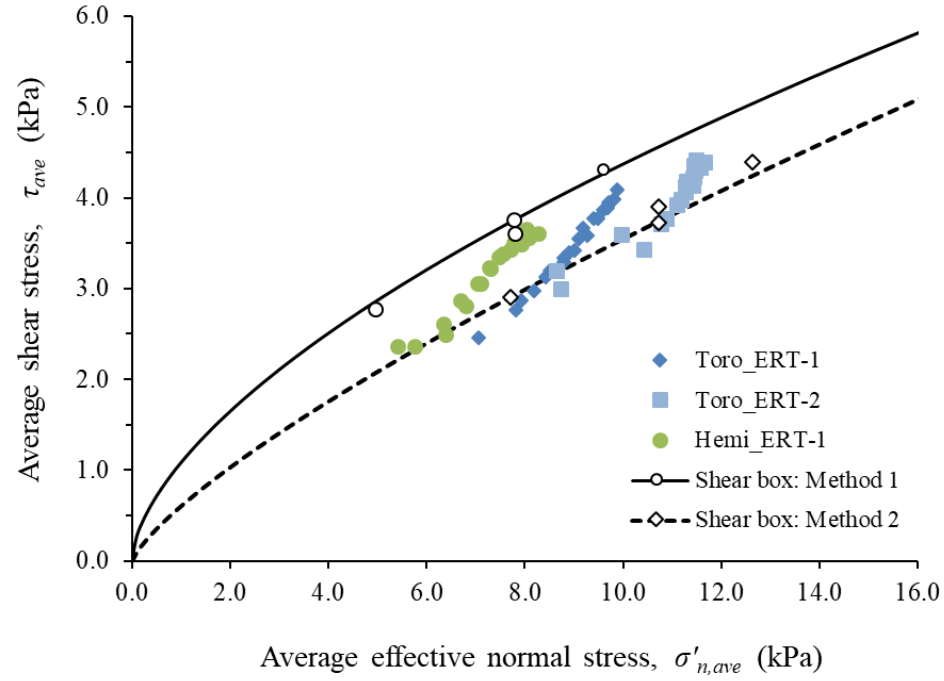

(c)

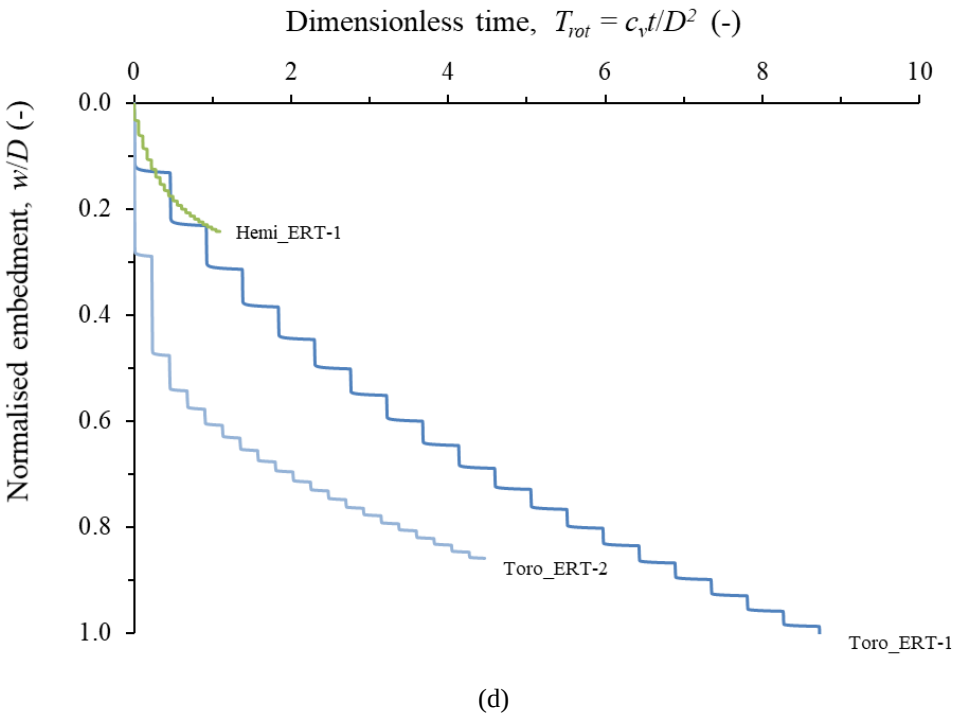

(d)

Figure 8: Results of episodic rotation tests: (a) normalised axial friction with dimensionless time; (b) interface friction with dimensionless time; (c) effective stress interpretation; and (d) embedment depth with time for all tests presented.

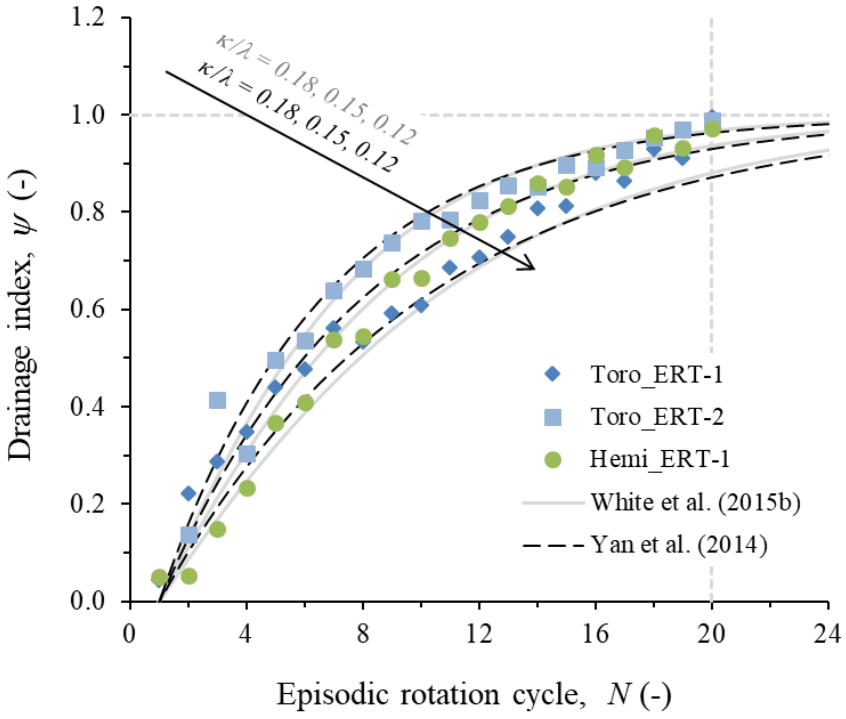

Figure 9: Episodic rotation test: cycle number vs. drainage index.

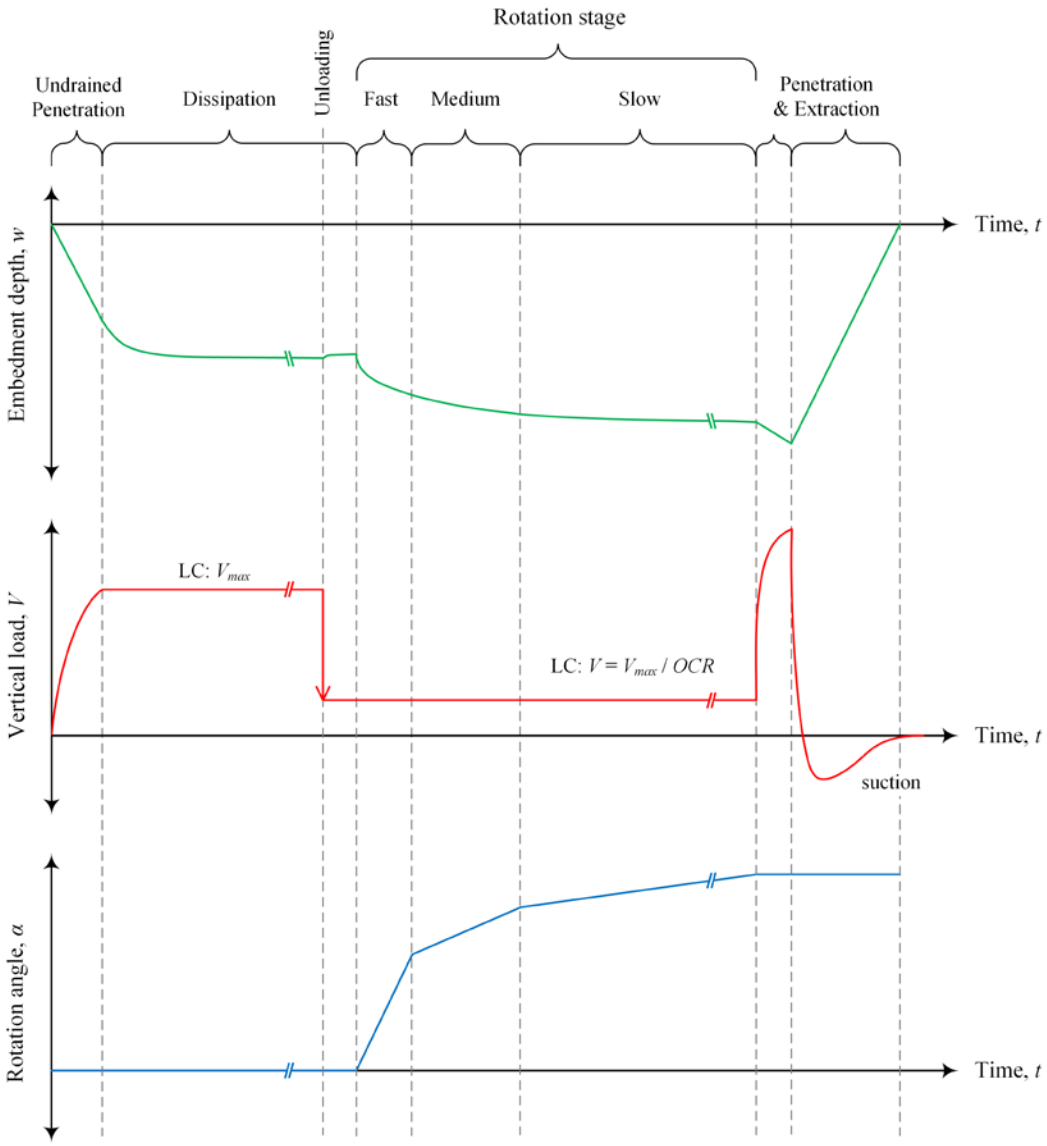

Figure 10: OCT test –penetrometer embedment, vertical load and rotation angle histories.

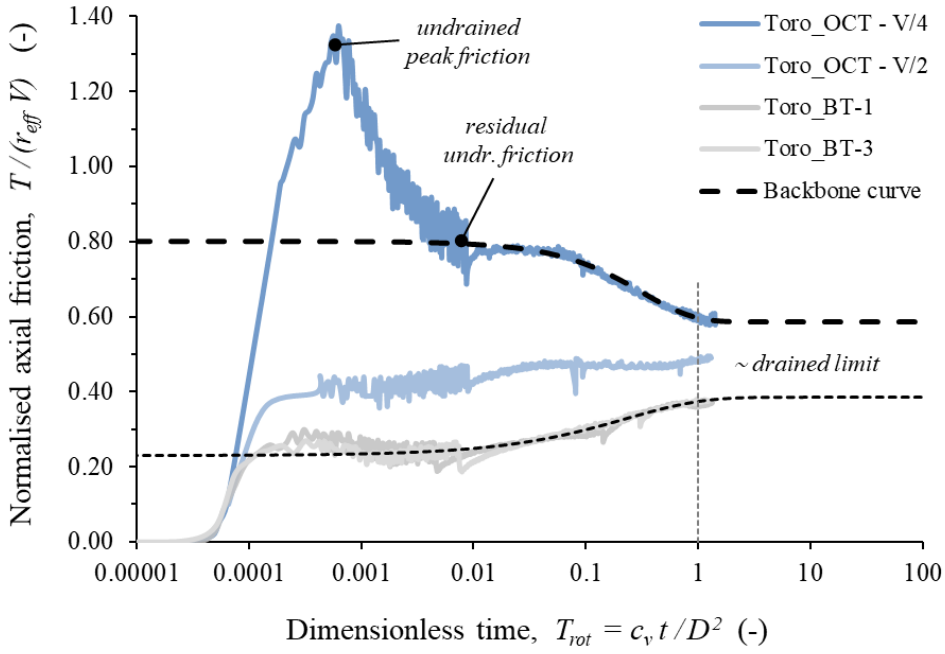
Normalised axial friction, $T/(r_{eff}V)$ (-)
1.40
1.20
1.00
0.80
0.60
0.40
0.20
0.00
undrained peak friction
residual undr. friction
~ drained limit
Toro_OCT - V/4
Toro_OCT - V/2
Toro_BT-1
Toro_BT-3
Backbone curve
0.00001
0.0001
0.001
0.01
0.1
1
10
100
Dimensionless time, $T_{rot} = c_v t/D^2$ (-)

(a)

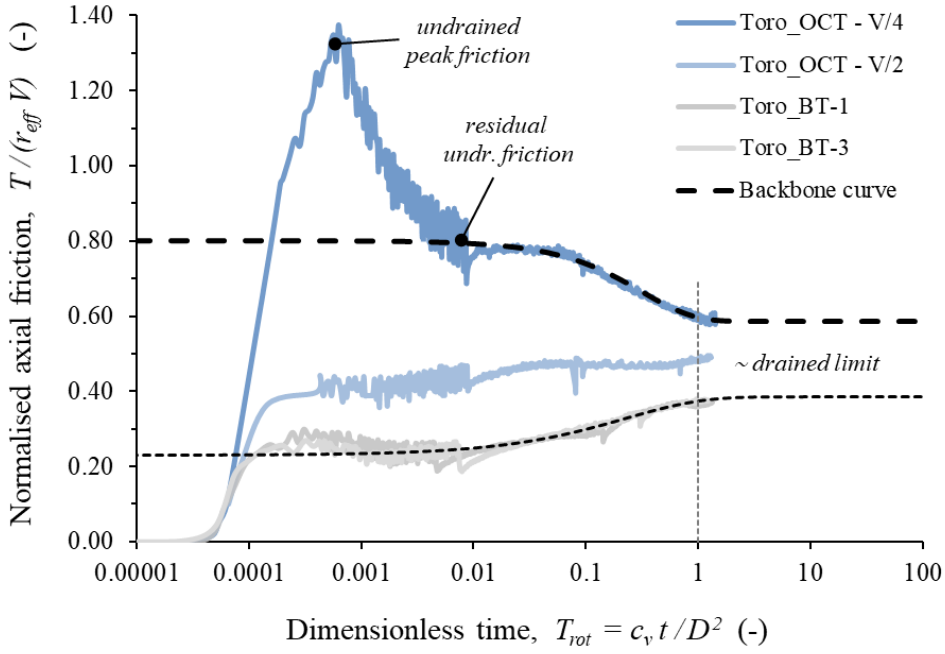
Normalised axial friction, $T/(r_{eff}V)$ (-)
1.40
1.20
1.00
0.80
0.60
0.40
0.20
0.00
undrained peak friction
residual undr. friction
~ drained limit
Toro_OCT - V/4
Toro_OCT - V/2
Toro_BT-1
Toro_BT-3
Backbone curve
0.00001
0.0001
0.001
0.01
0.1
1
10
100
Dimensionless time, $T_{rot} = c_v t/D^2$ (-)

(b)

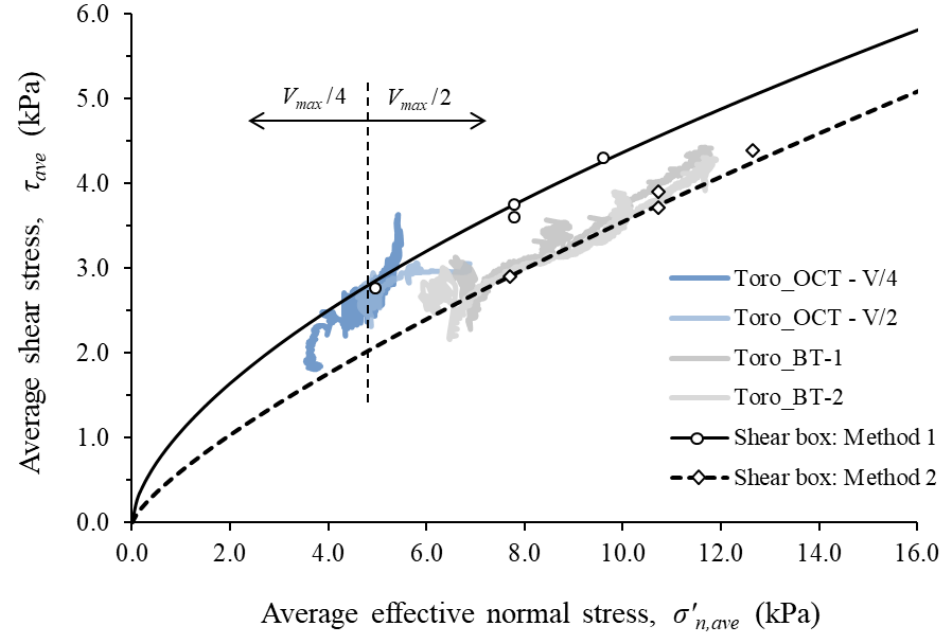

(c)

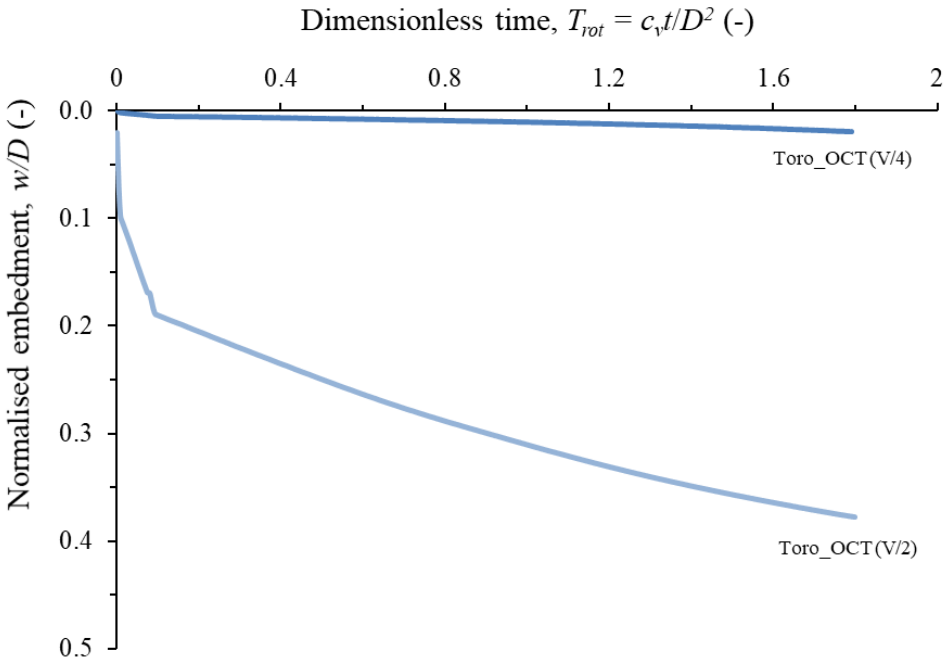

(d)

Figure 11: Results of over-consolidation ratio tests for the toroid penetrometer: (a) normalised axial friction with dimensionless time; (b) interface friction with dimensionless time; and (c) effective stress interpretation; and (d) embedment depth with time for all tests presented.

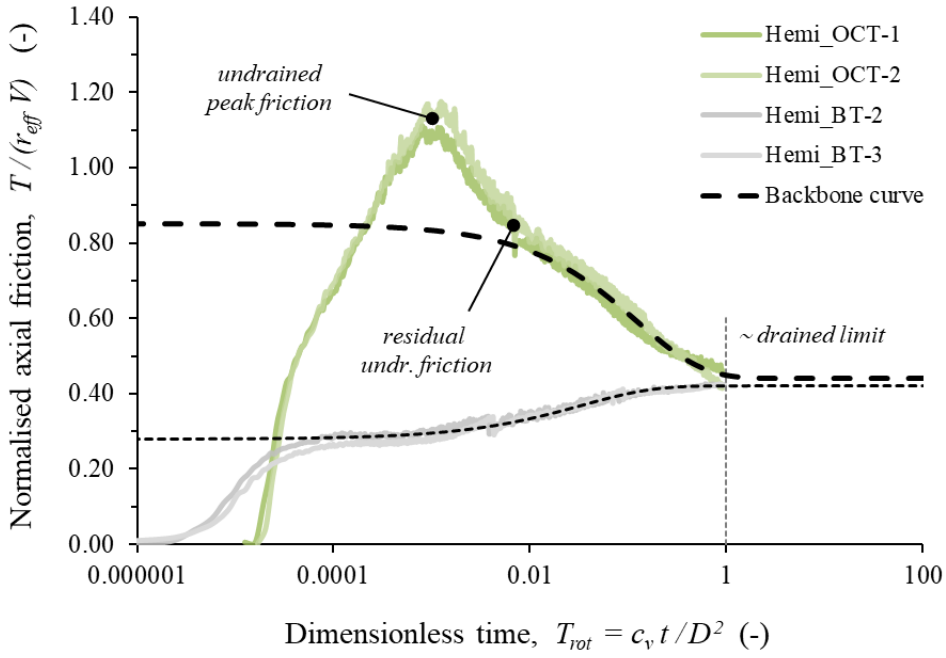
Normalised axial friction, $T/(r_{eff}V)$ (-)
1.40
1.20
1.00
0.80
0.60
0.40
0.20
0.00
0.000001
0.0001
0.01
1
100
Dimensionless time, $T_{rot} = c_v t/D^2$ (-)
Hemi_OCT-1
Hemi_OCT-2
Hemi_BT-2
Hemi_BT-3
Backbone curve
undrained peak friction
residual undr. friction
~ drained limit

(a)

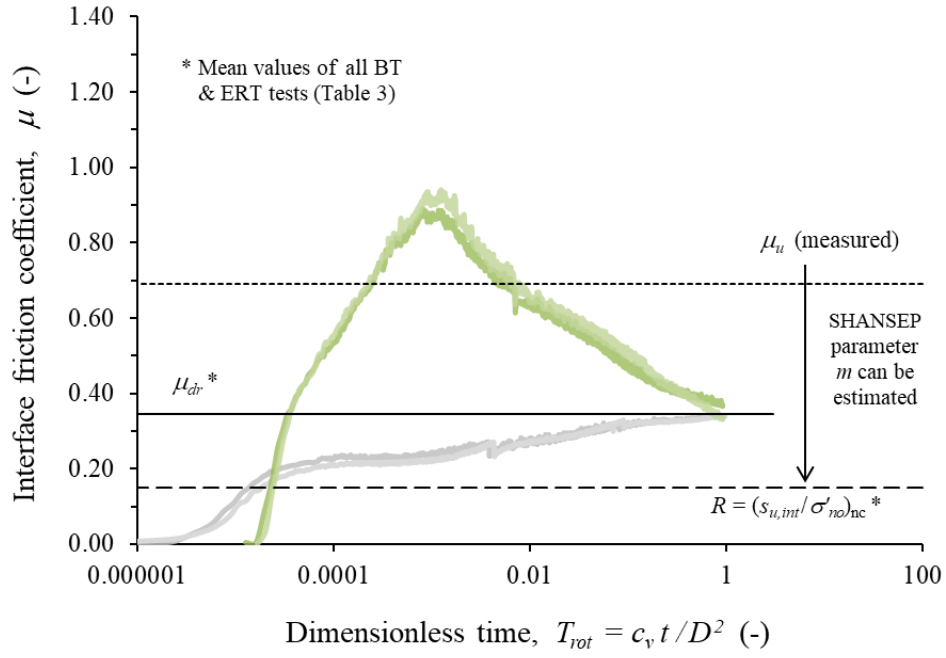
Interface friction coefficient, μ (-)
1.40
1.20
1.00
0.80
0.60
0.40
0.20
0.00
0.000001
0.0001
0.01
1
100
Dimensionless time, $T_{rot} = c_v t/D^2$ (-)
* Mean values of all BT & ERT tests (Table 3)
μ_u (measured)
SHANSEP parameter m can be estimated
μ_{dr} *
$R = (s_{u,int}/\sigma'_{no})_{nc}$ *

(b)

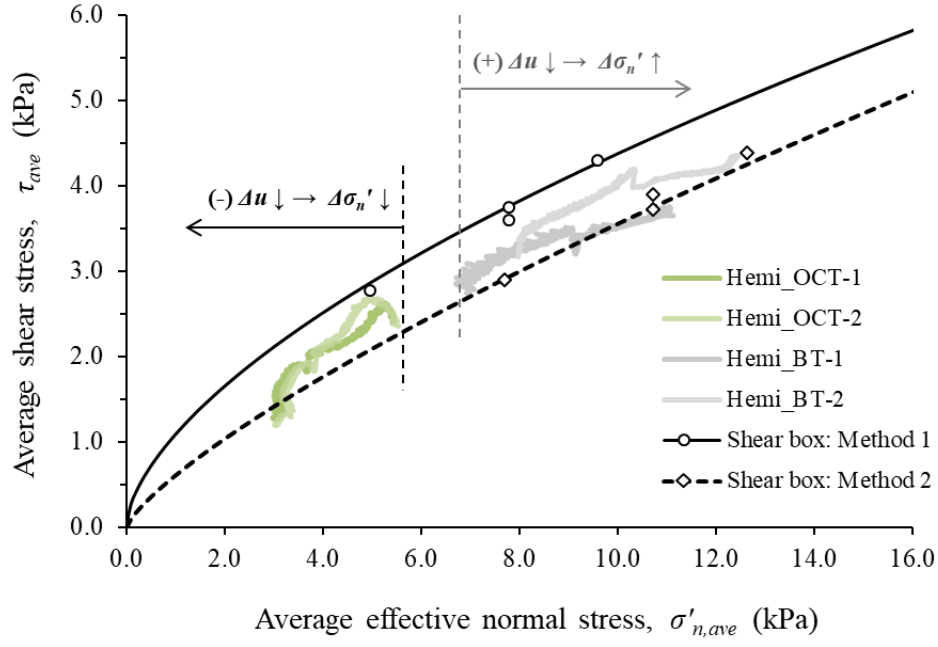

(c)

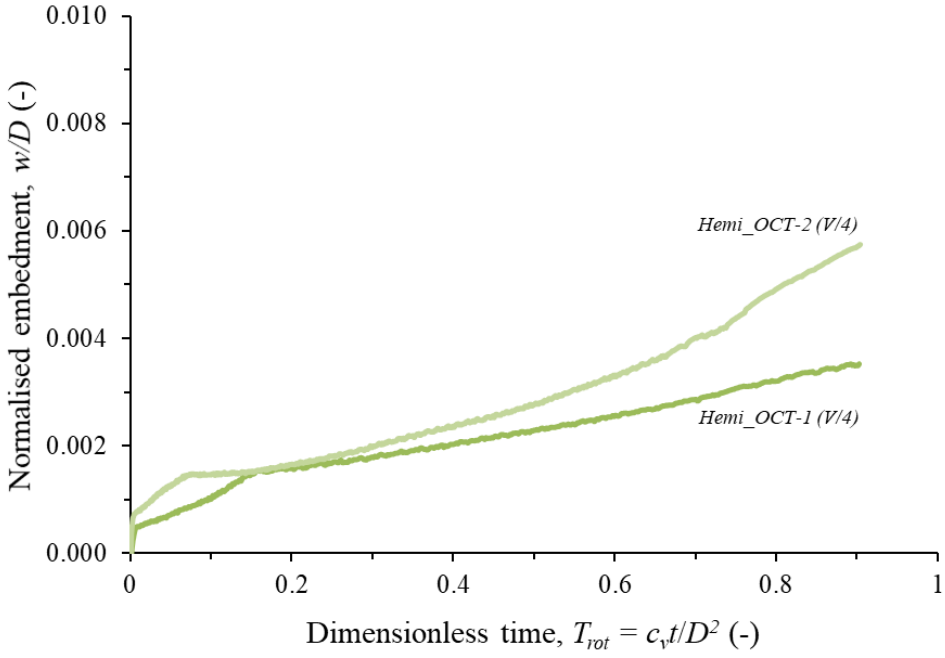

(d)

Figure 12: Results of over-consolidation ratio tests for the hemiball penetrometer: (a) normalised axial friction with dimensionless time; (b) interface friction with dimensionless time; and (c) effective stress interpretation; and (d) embedment depth with time for all tests presented.

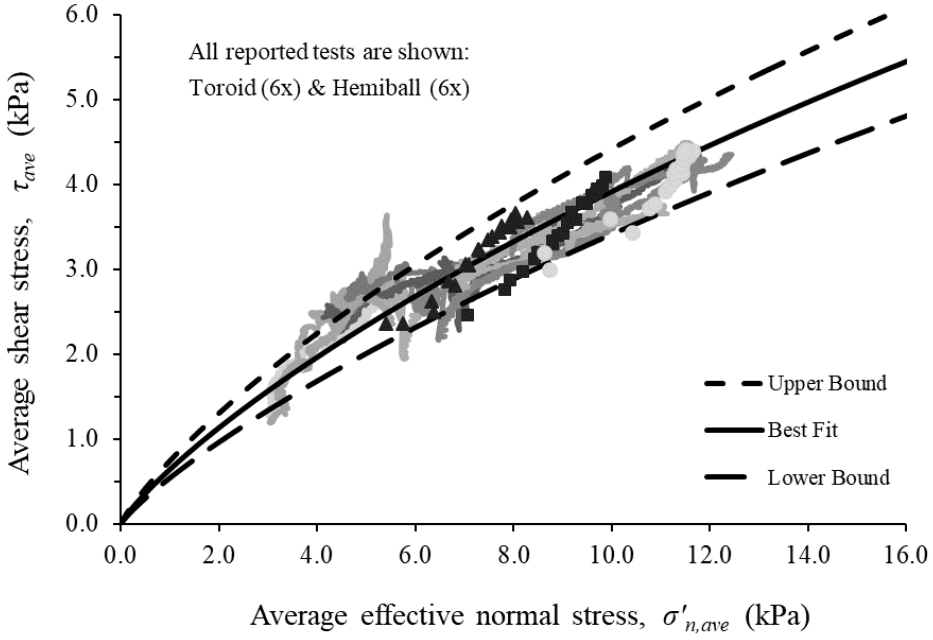

(a)

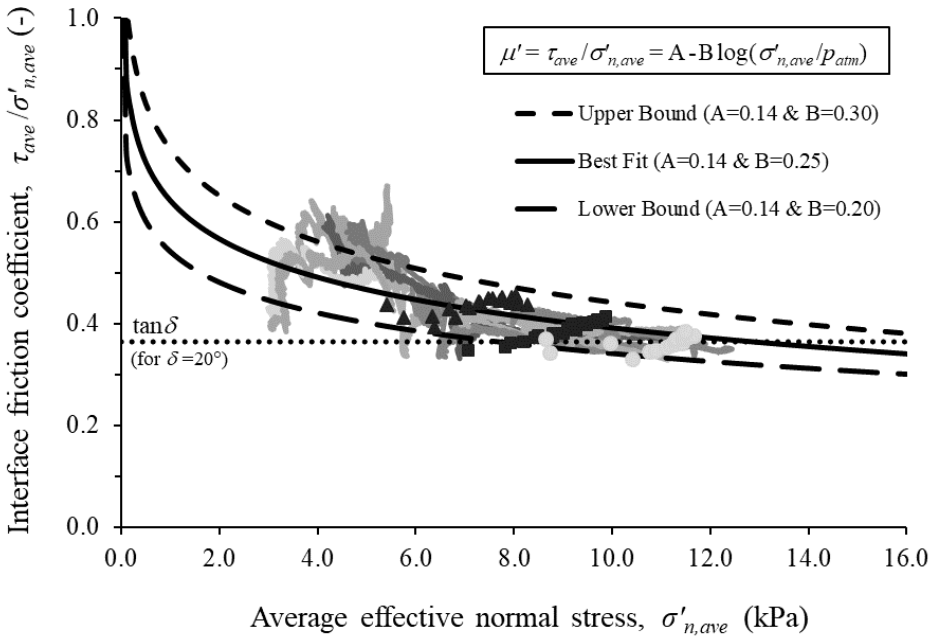

(b)

Figure 13: Summary of shallow penetrometer tests in effective stress space: (a) effective stress envelopes; and (b) effective interface friction.